Topological transmission in Suzuki-phase sonic crystals

Zhen Huang,[1,2] Francisco Cervera,[1] Jiu Hui Wu,[2,*] Martin Ibarias,[1] Chongrui Liu,[2]
Victor M. García-Chocano,[1] Fuyin Ma,[2,†] and José Sánchez-Dehesa[1,‡]

[1] *Wave Phenomena Group, Department of Electronic Engineering, Universitat Politècnica de València, Camino de vera s.n. (Building 7F), Valencia, ES-46022, Spain*
[2] *School of Mechanical Engineering, Xi'an Jiaotong University, Xi'an 710049, China*

(Received 10 November 2023; revised 23 February 2024; accepted 29 March 2024; published 2 May 2024)

This work reports extraordinary topological properties of sound transmission through topological states in sonic crystals denominated by the Suzuki phase, consisting of a rectangular lattice of vacancies created in a triangular lattice. These low-symmetry crystals exhibit unique properties due to the embedded lattice of vacancies. A generalized folding method explains the band structure and the quasi-type-II Dirac point in the Suzuki phase, which is related to the underlying triangular lattice. Analogous to the acoustic valley Hall effect, the Suzuki phase contains three types of topological edge states on the four possible interfaces separating two Suzuki-phase crystals with distinct topological phases. The edge states have defined symmetries with inherent directionality, which affect the topological sound transmission and are different from chirality, valley vorticity, or helicity. Particularly, the existence of topological deaf bands is reported here. The propagation of topological eigenmodes on the same interface is also different; this is quantified using the acoustic Shannon entropy, making the topological transport dependent on the frequency of the edge states. Based on the abundant topological edge states of Suzuki-phase crystals, a multifunctional device with acoustic diodes, multichannel transmission, and selective acoustic transmission can be designed. Numerical simulations and measurements demonstrate the topological transmission. Our work extends the research platform of acoustic topological states to lattices with low symmetry, which opens avenues for enriching topological states with broad engineering applications.

DOI: 10.1103/PhysRevApplied.21.054003

I. INTRODUCTION

The discovery of the quantum Hall effect has opened a new field of research in condensed-matter physics, where topology describes the global behavior of energy bands in the momentum space [1,2]. The investigation of topological phases of matter triggered fundamental discoveries, such as the quantum spin Hall effect [3,4], three-dimensional topological insulators [4,5], valley Hall insulators [6–8], crystalline insulators [9,10], and topological semimetals [11,12]. Motivated by the exotic properties of edge states, supporting transport immune to backscattering, and the development of a topological phase in condensed-matter systems, such topological physics concepts have been extended to classical wave systems, including photonics [13–16], acoustics [17–23], and mechanics [24–27], to realize different topological states for wave manipulation.

For two-dimensional (2D) topological acoustic systems, the emergence of quite a few topological edge states is associated with the existence of type-I Dirac points (DPs) [28,29], which are characterized by two fundamental features (i.e., double degeneracy and linear dispersion near the degenerate point) and guaranteed to exist at the corners of the first Brillouin zone (FBZ) due to the symmetry of the lattice [28,30,31]. For example, according to group theory, the lattice with the C_{6v} (or C_{3v}) group, which has 2D E_1/E_2 representation, can guarantee the presence of type-I DPs in the FBZ associated with time-reversal symmetry [21,30,32,33]. Breaking the DP can lead to the emergence of topology-related effects in acoustic systems. For example, by employing a circular flow into the fluid-filled region arranged in a hexagonal lattice or a honeycomb lattice [18,34], the degeneracy can be lifted without time-reversal symmetry due to the induced acoustic nonreciprocity [18]. The nonzero Chern number for the bands below the opened gap implies that the system supports an acoustic quantum Hall effect [19]. In addition to introducing external dynamic components into the crystal, the structure of the unit cell can also be changed to break the DPs. One typical strategy is a rotation-scattering mechanism to break the inversion or mirror symmetry [35,36]. Time-reversal symmetry leads to the zero Chern number, when calculating the Berry curvature over the full FBZ. However, there are

*Corresponding author: ejhwu@xjtu.edu.cn
†Corresponding author: xjmafuyin@xjtu.edu.cn
‡Corresponding author: jsdehesa@upv.es

strong peaks of the Berry curvature appearing near the corners of the FBZ; these give rise to the acoustic valley Hall effect [35]. Interestingly, the DPs can be superimposed [21,22]. Besides, a single Dirac cone can be combined into a double cone through band folding [37] or accidental degeneracy [38]. The two degenerate modes can be hybridized to create the acoustic pseudospin states; in this way, the acoustic quantum spin Hall effect, characterized by the pseudospin-dependent one-way transport of sound edge states localized at the domain walls, can be realized [38]. It is worth noting that the platforms studied above are lattices with high symmetry, such as triangular, honeycomb, kagome, or square lattices [20,28,39]. Moreover, topologically protected edge states usually occur on one boundary, such as zigzag boundaries of triangular lattices and honeycomb lattices. Therefore, the question naturally arises for a general lattice, such as the rectangular lattice with low symmetry, of whether or not there are topological edge states in the case of double-degeneracy points without the limit of type-I DPs. Moreover, what are the distinct features of the edge states if they exist?

Here, we studied a rectangular lattice with low symmetry, known as the acoustic Suzuki phase (ASP). By employing the generalized band-folding method, we explained the band structure of the Suzuki phase and discovered that it supported an accidental quasi-type-II DP in the band structure when the scatterers had a certain dimension. Drawing an analogy with the acoustic valley Hall effect, we confirmed the existence of quantized valley indices in systems with broken DPs, which could be utilized to obtain topological edge states located on the interfaces separating two systems with distinct topological phases. Numerical simulations demonstrate that both horizontal and vertical supercells with different interfaces support topological states simultaneously, with the eigenmodes of the topological states exhibiting well-defined symmetry. This unique property has implications for topological sound transmission, including the emergence of topological deaf bands. The acoustic Shannon entropy of eigenmodes indicates that, even for topological states on the same type of domain wall, their degrees of localization vary, leading to changes in topological sound transmission. This wealth of topological information can be harnessed to construct versatile acoustic devices, such as acoustic diodes, multichannel, sound-source recognition, and selective sound transmitters. Additionally, simulations and measurements demonstrate the topological transmission.

II. ACOUSTIC SUZUKI PHASE AND DEGENERATE POINT

A. Two-dimensional acoustic Suzuki phase

In the study of the physical properties of alkali halides, Suzuki found that some of them, after being doped with divalent cations, produced a new ionic compound, which had periodically distributed vacancies, and the lattice period was roughly twice the original one. On the basis of maintaining the properties of the original compound, the new compound exhibits properties specifically attributed to the lattice of vacancies [40]. Inspired by this finding, Caballero *et al*. introduced the sonic crystal (SC) lattice denominated acoustic Suzuki phase [41], the scattering properties of which combined the properties of the underlying triangular lattice and that of the lattice of vacancies.

Figure 1(a) shows a three-dimensional (3D) view of the actual 2D ASP crystal under study in this work. This crystal can be described as a rectangular lattice with lattice vectors $\mathbf{a}_1$ and $\mathbf{a}_2$, and a basis to three identical cylindrical scatterers with a triangular section. Due to the absence of any rotational symmetry in the unit cell of the ASP, except for the identity operation [42], the ASP exhibits low symmetry. The radius of the circumscribed circle of the triangular scatterers is R. The central points of the four triangular prisms form a rhombus with an included angle $\gamma = 60^\circ$ and side length a, and the center of the rhombus coincides with the center of the cell at point O. The primitive vectors of the unit cell are $\mathbf{a}_1 = 2a\hat{\mathbf{x}}$ and $\mathbf{a}_2 = a\sqrt{3}\hat{\mathbf{y}}$. The reciprocal space and its corresponding FBZ, which is rectangular, are plotted in Fig. 1(a). The four symmetry points in the FBZ are $\Gamma = (0, 0)$, $X = (\pi/2a, 0)$, $L = \left(\pi/2a, \pi/\left(a\sqrt{3}\right)\right)$, and $Y = \left(0, \pi/\left(a\sqrt{3}\right)\right)$, which define the irreducible Brillouin zone (BZ).

Figure 1(b) shows the dispersion relation of the modes propagating in the ASP with parameters $a = 50$ mm and $R = 0.56a$. The acoustic band structure (see Appendix A), which is represented along the high-symmetry directions of the irreducible BZ, exhibits pseudogaps (blue and yellow stripes) in both the Γ-X and Γ-Y directions [41]. The formation of pseudogaps observed between the first and second bands is directly related to the lattice of vacancies existing in the ASP structure [41]. Since these pseudogaps overlap in a narrow band of frequencies, a complete band gap (red stripe) occurs at low frequencies. A nodal point exits between the third and fourth bands, which is an accidental degeneracy point emerging at the low-symmetry point in reciprocal space and supporting valley Hall kink states, known as a type-II Dirac point [28,43,44], as shown by the red dot (D-II) in Fig. 1(b). More interestingly, the fourth and fifth bands are almost degenerate near point X, as shown in the magnification [dashed box in Fig. 1(b)]. By altering the structural parameters of the unit cell to modulate the sound-field distribution, the double-degeneracy point (DDP) can be realized between the fourth and fifth bands. Figure 1(c) shows the position of the $\mathbf{k}$ wavevector in the Γ-X direction, where the DDP appears as a function of filling ratio *R/a.* Numerical calculations show that, when *R*/*a* is not greater than 0.55, the DDP will appear in the fourth and fifth bands. When the filling ratio decreases, the position of the DDP gradually moves away

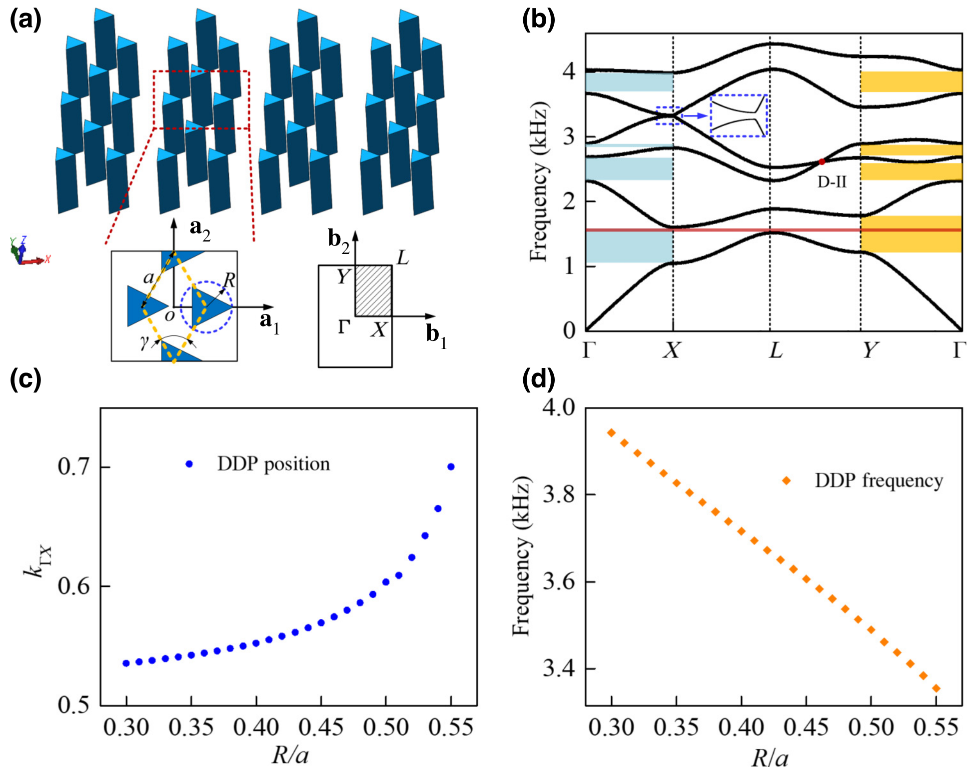

FIG. 1. (a) 3D view of Suzuki-phase crystal under study. One of the two insets shows a magnified view of the 2D unit cell with lattice vectors $\mathbf{a}_1$ and $\mathbf{a}_2$. Centers of the four triangular cylinders, the circumcircle radius of which is R, form a rhombus with side length a, and the rhombus angle, γ, is 60°. In addition, the center of the rhombus coincides with the center of the Suzuki-phase cell at point O. Other inset shows the FBZ of the Suzuki phase, where vectors $\mathbf{b}_1$ and $\mathbf{b}_2$ are the lattice vectors of the reciprocal lattice and the rectangle ΓXLY defines the irreducible BZ. (b) Dispersion relation of an ASP cell. Blue shading indicates the band gap in the Γ-X direction, and the yellow area indicates the band gap in the Γ-Y direction. Red shading indicates the complete band gap. Dotted boxes indicate magnified views of bands near point X. (c) Relationship between the position of DDP in k space and the ratio of R/a. Since the length ratio of ΓX and XL is 0.75, the relative length of ΓX is 0.75 when the relative length of XL is taken as $\sqrt{3}/2$. (d) Relationship between the frequency of DDP and the ratio of R/a.

from point X. Due to the interaction between the sound field and the scatterers being weakened, the frequency of the DDP is increased, as shown in Fig. 1(d). Note that during the process of reducing the filling ratio, the change in the sound-field distribution causes the fifth and sixth bands to exhibit a crossing phenomenon [45], which can lead to the emergence of an indirect band gap after opening of the DDP, especially when R/a is less than 0.3, the indirect band gap may not exist. However, different from the type-I DP at the corners of the FBZ due to crystal symmetry, the accidental DDP formed by the fourth and fifth bands in the ASP is located at the low-symmetry point in the FBZ, and the cone related to the DDP lacks obvious tilted features in a specific direction [28,43]. Therefore, it can be referred to as a quasi-type-II DP.

B. Generalized band-folding method and degenerate point

The quasi-type-II DP in the Suzuki phase is related to the type-I DP in the triangular lattice (see Appendix B for details). To reveal their relationship, we have folded the irreducible BZ of the triangular lattice into the irreducible BZ of the rectangular lattice. Figure 2(a) describes the folding method, which folds the discrete FBZ (blue region) of the triangular lattice into the smaller FBZ (green region) of the rectangular lattice. Due to the symmetry [37], the folding process can be simplified as folding region $\Gamma PK'K\Gamma$ (including three irreducible BZs for the triangular crystal) into region ΓXGY (containing one irreducible BZ for the ASP). The specific process is as follows. In the first step, considering the different geometric shapes of the two areas, we have developed a method to split and classify the area to be folded into the smaller irreducible BZ. Thus, the boundary lines of the reference area (ΓXGY) are extended to intersect the large irreducible BZ at points P, Q, and M, respectively. To obtain a simple geometric figure, draw vertical lines at the K' and M points, and the intersection points are S and N, respectively. Through this division, the area to be folded is divided into basic geometrical shapes. Through simple algebraic operations,

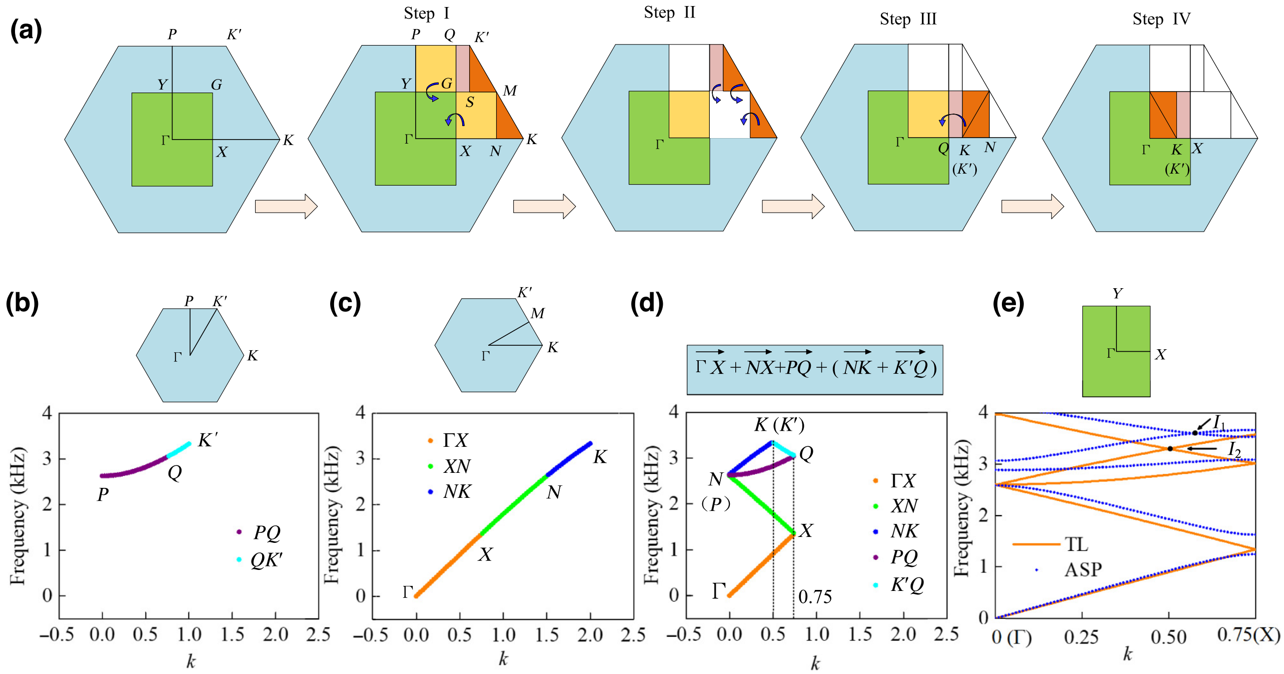

FIG. 2. (a) Sketch of the procedure showing folding of the irreducible BZ of the triangular lattice into the one corresponding to the Suzuki-phase lattice. Blue and green areas represent the FBZ of the triangular lattice and the FBZ of the Suzuki phase, respectively. Yellow areas indicate the first level of folding, red areas indicate the second level of folding, and purple indicates the third level. Circular arrows indicate the direction of folding. (b) Dispersion relation of the triangular lattice along the $\overrightarrow{PK'}$ boundary. Q point belongs to the $\overrightarrow{PK'}$ vector, and $|\overrightarrow{PQ}| = |\overrightarrow{\Gamma X}|$. (c) Dispersion relation along $\overrightarrow{\Gamma K}$ in the FBZ of the triangular lattice. Points X and N are in vectors $\overrightarrow{\Gamma K}$ and $|\overrightarrow{\Gamma X}| = |\overrightarrow{XN}|$. (d) First band includes modes along $\overrightarrow{PK'}$ and $\overrightarrow{\Gamma K}$ directions belonging to the $\Gamma PK'$ and ΓMK areas of the triangular lattice. (e) Dispersion relation of the ASP (dotted line) along the Γ-X direction (top panel) and the triangular lattice (TL, orange line). I_1 and I_2 represent the quasi-type-II DP in the ASP and the type-I DP in the triangular lattice, respectively.

$|\overrightarrow{\Gamma Y}| = |\overrightarrow{YP}| = \pi/\sqrt{3}a$ and $|\overrightarrow{\Gamma X}| = |\overrightarrow{XN}| = \pi/2a$. Therefore, the yellow areas in Fig. 2(a) define the largest regions folded along the boundary line into the reference area, and they completely cover it, as described in step II. Next, considering that the triangular areas (colored in red) and the rectangular area (colored in purple) are not in contact with the boundaries of the reference area, they need to be folded into the first-level area (yellow area) first. Since $|\overrightarrow{NK}| = |\overrightarrow{SM}| = \pi/3a$ and $|\overrightarrow{GS}| = \pi/6a$, step III in the process consists of folding the triangular and rectangular areas into the first-level area, as shown in Fig. 2(a). The process ends with step IV, in which the rectangular and triangular areas, already folded in the previous step, are folded again into the reference area, thereby finishing the folding process of the BZ of the triangular lattice into the irreducible BZ of the ASP lattice. In this process, the $\overrightarrow{\Gamma X}$ boundary of the Suzuki BZ is composed of vectors $\overrightarrow{\Gamma X}$, $\overrightarrow{NX}$, $\overrightarrow{PQ}$, $\overrightarrow{NK}$, and $\overrightarrow{K'Q}$ in the FBZ of the triangular lattice. To further demonstrate the process of band folding, we study the first band in the FBZ of the triangular lattice. Figure 2(b) shows the dispersion relation along the $\overrightarrow{PK'}$ vector in the boundary of the FBZ of the triangular lattice. According to the geometric relationship, $|\overrightarrow{PQ}| = |\overrightarrow{\Gamma X}|$, and the acoustic bands along $\overrightarrow{PQ}$ and $\overrightarrow{QK'}$ are represented by purple and cyan curves, respectively. Similarly, Fig. 2(c) provides the dispersion relations of $\overrightarrow{\Gamma X}$, $\overrightarrow{XN}$, and $\overrightarrow{NK}$ in the direction of the $\overrightarrow{PK'}$ boundary vector, which are indicated by orange, green, and blue curves, respectively. According to the band-folding procedure previously described, $\overrightarrow{\Gamma X}$, $\overrightarrow{NX}$, $\overrightarrow{PQ}$, $\overrightarrow{NK}$, and $\overrightarrow{K'Q}$ are sequentially added to the graph shown in Fig. 2(d). Orange lines in Fig. 2(e) show the band structure (along the Γ-X direction of the FBZ) of the triangular lattice. It is compared with that of the ASP lattice (blue dotted lines) with $R = 0.54a$. It is observed that the frequency of point I_1 in the ASP lattice has been shifted up in frequency with respect to the frequency of point I_2 in the triangular lattice.

Different from the band-folding method usually employed in reducing BZs with similar geometrical shapes [28,46,47], the method developed here can be generalized to BZs with arbitrary shapes and it is more universal. And when there are 2D irreducible representations in the point-group symmetry of the triangular lattice, this kind of quasi-type-II Dirac point is also guaranteed in other classical systems, such as photonic crystals with the Suzuki phase. In addition, from the band-folding process, we infer that the quasi-type-II DP in the ASP lattice is related to the type-I DP appearing at the corners of the BZ in the triangular lattice, so it has the characteristics of an energy valley, which is the underlying physics for achieving topological states in the ASP lattice.

III. TOPOLOGICAL STATES OF THE ACOUSTIC SUZUKI PHASE

A. Topological phase of the acoustic Suzuki phase

Section II has shown that the presence of the quasi-type-II DP is secured when $R \leq 0.55a$. In addition, their frequencies decrease when the dimension of the triangular rods increases. Without loss of generality, the results reported in this section are obtained using $R = 0.54a$. Solid lines in Fig. 3(a) show the band structure corresponding to the ASP unit cell described in the bottom inset, where the rotation angle of the rods is $\beta = 30°$. The two dotted blue lines represent the fourth and fifth bands where the rotation angle of the rods is 0° (see the upper inset). The two bands form the quasi-type-II DP (I_1), as shown in the red box in Fig. 3(a). The yellow stripes indicate the complete band gaps, which are associated with the lattice of vacancies defining the ASP [41]. Particularly, $Sg1$ denotes the lowest band gap. The simulations also indicate that I_1 occurs at the wavevector $k = 0.6695$, near the X point ($k = 0.75$) of the irreducible BZ. The rotation of the triangular rod can modify the band structure and remove the band degeneracy observed at I_1 [35]. Therefore, we have studied the behavior of the two modes involved in the quasi-type-II DP against a rotation period of the triangular rod, from $-60°$ to 60°. Figure 3(b) shows the results obtained, showing that the mode frequencies change with rotation angle β, undergoing a cycling process of opening, closing, and opening again, which is similar to the topological transition [48]. However, the two low-frequency band gaps (orange stripes) do not undergo any band-gap closing during this rotation process. In addition, when $|\beta| = 30°$, the band-gap width formed by degeneracy lifting is the largest. The SCs made of rods with rotation angles $-30°$ and $+30°$ are named SC-A and SC-B, respectively. Figure 3(c) shows

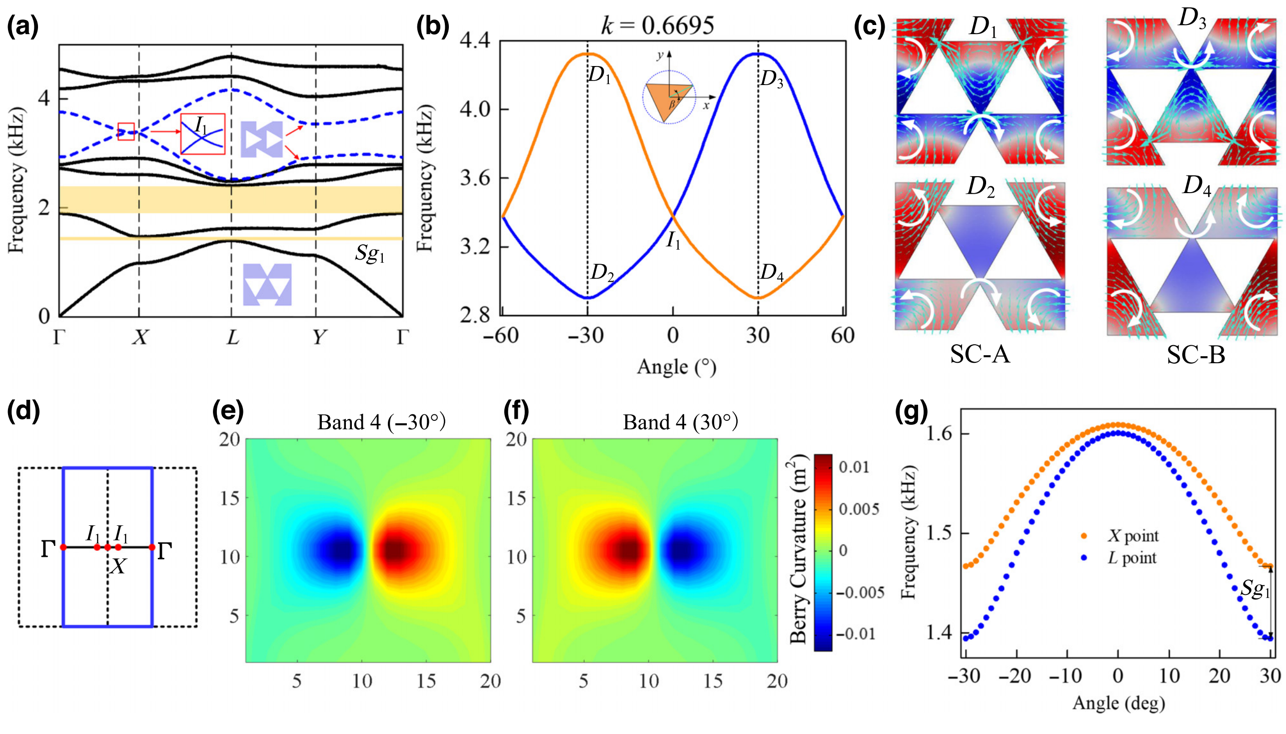

FIG. 3. (a) Band structure for the ASP lattice with $R = 0.54a$. Solid lines indicate the dispersion relation with $\beta = 30°$ (see the bottom inset). Dashed lines depict the fourth and fifth bands obtained with the unit cell shown in the top inset, where the triangular rods are rotated 0°. Yellow stripes indicate the complete band gaps, where Sg_1 denotes the lowest-frequency band gap. (b) Dependence on the rod rotation angle (β) of the frequency of the quasi-type-II DP. Blue and orange solid lines represent the two modes involved in the DP. Inset defines rotation angle β. (c) Pressure patterns of modes obtained when rods are rotated $\pm 30°$. Red and blue colors denote positive and negative values, respectively. White circular arrows represent the flux of acoustic energy. (d) FBZ of the ASP lattice. Dotted rectangles indicate two adjacent FBZs, and the solid-line rectangle indicates the FBZ constructed from the center Γ point of two adjacent FBZs. (e),(f) Berry curvature distributions of the fourth band for rotation angles $-30°$ and $+30°$ respectively. (g) Rotation dependence of the frequencies at the L point of the first band (blue dotted line) and at the X point of the second band (orange dotted line). Separation between both frequencies defines the band-gap width, Sg_1.

snapshots of the pressure patterns calculated for $D1$–$D4$ after removing the frequency degeneracy. All the patterns exhibit mirror symmetry with respect to the Y-Z plane. From the acoustic energy flow, which is represented by the white circular arrows, it is observed that, unlike the classical valley-mode exchange energy, the modes of $D1$ ($D2$) and $D4$ ($D3$) are not the same. This is caused by two main factors; one is the different lengths of the primitive vectors defining the rectangular lattice. The other is that there is an acoustic vortex at the apex of the truncated triangular rod due to the specific shape of the rod. The energy vortex is related to the shape of the truncated rod; for example, $D1$ and $D2$ in SC-A are both clockwise, while $D3$ and $D4$ in SC-B are both counterclockwise.

The system with nontrivial topological properties can usually be quantified with an invariant, a mathematical quantity that cannot change upon continuous deformations [4,25]. Since the quasi-type-II DP in the ASP is obtained by band folding of the triangular lattice, we use the valley Chern numbers related to the acoustic valley Hall effect to characterize the topological phases of SC-A and SC-B. We calculate the valley Chern number of the SC in the FBZ shown in Fig. 3(d), which can be obtained by integrating the Berry curvature, $\mathbf{F}_n(\mathbf{k})$, over the $\mathbf{k}$ space in the 2D torus [49]. For example, for the nth energy band in the frequency-band structure, the formula for calculating its Chern number, C_n, can be defined as $C_n = (1/2\pi) \iint \mathbf{F}_n(\mathbf{k}) d^2\mathbf{k}$ [50,51]. To facilitate the calculation, the torus is discretized into the same coordinate blocks, and then within each block, the same $U(1)$ canonical transformation can be used [50,52]. Under this transformation, the distribution of the Berry curvature on the target band over the entire discrete BZ can be obtained (see Appendix C for details). Figures 3(e) and 3(f) show the Berry curvature [actually $\mathbf{F}_n(\mathbf{k})/(2\pi)$] distributions on the fourth band of SC-A and SC-B, respectively, in momentum space, where the Berry curvature is mainly located around point I_1. Note that they exhibit opposite signs (represented by different colors). Therefore, its integral over the full Brillouin zone is zero, while, for the left half of the BZ of SC-A, the integral of the Berry curvature within point I_1 is $-1/2$. The Berry curvature integral result of SC-B is 1/2, which is the same as that of the acoustic valley state [53].The valley Chern number differences on both sides of the interface are quantized, $|\Delta C_4| = |C_4(\text{SC - A}) - C_4(\text{SC - B})| = 1$. This indicates that SC-A and SC-B have different topological phases, so there will be topologically protected edge states at the interface composed of SC-A and SC-B, while there are no edge states on the interface composed of the same topological phase (see Appendix D). In addition, we calculate the frequency variation at high-symmetry points X and L in the BZ on the first and second bands within half a rotation cycle of the rod (from $-30°$ to $30°$), as shown in Fig. 3(g). The difference between both frequencies defines the band-gap width, Sg_1, which increases with the absolute value of the rotation angle, $|\beta|$. Thus, in the ASP, the band gap associated with the lattice of vacancies can be further widened by the rotation-rod mechanism.

For the case of the acoustic valley Hall effect, spatial inversion symmetry breaking gaps between inequivalent K and K' in the FBZ give rise to band inversion [35]. In the ASP crystal, the quasi-type-II DP is obtained by the band-folding method, and the position of the DP in momentum space is variable. Besides, in the process of band flipping of insulators supporting the acoustic valley Hall effect, a pair of eigenmodes formed by lifting the degenerate point are simply flipped [54], while the case for the ASP is different, due to modulation by the scatterer geometry, this pair of eigenmodes displays special symmetry. Based on these differences, the topological states obtained on the domain walls of the ASP can be regarded as valleylike edge states.

B. Superlattice band structure and topological edge states

To verify the existence of topological edge states in the ASP, we construct several supercell structures combining SC-A and SC-B. Different from the case of triangular, honeycomb, and square lattices, the interfaces of the supercell structure composed of such crystals can be divided into two types, according to the distribution of SCs on both sides of the interface. That is, the cells in the supercell are arranged vertically (the number of horizontal cells is 1), and the cells in the supercell are arranged horizontally (the number of vertical cells is 1). Combined with the shape of the sonic crystals on both sides of the interface, each kind of supercell structure can be subdivided into two types. The interfaces contained in the vertical supercell are called interface I and interface III, while the interfaces of the horizontal supercell are named interface II and interface IV.

Figure 4(a) schematically depicts the case of a vertical supercell containing interface I composed of SC-A (upper) and SC-B (lower), and interface III composed of SC-A (lower) and SC-B (upper). The supercell contains 40×1 cells, of which both ends contain 10×1 cells. The magnified view of this interface (red dashed rectangle) shows that it contains a rhomboid structure composed of two triangular rods. The magnified view of interface III (red dashed rectangle) shows that interface III contains a heteromorphic structure consisting of two trapezoidal rods. The different heterotypic structures on interfaces I and III indicate that the projected bands are also different. Floquet periodic boundary conditions are applied at the left and right boundaries of the supercell, and both ends of the supercell are set as continuous boundaries.

Figure 4(b) shows the projected band structure of the vertical supercell. There are two kinds of edge states; the blue (ES-I) and orange (ES-III) lines represent the states on interfaces I and III, respectively, which lie within the

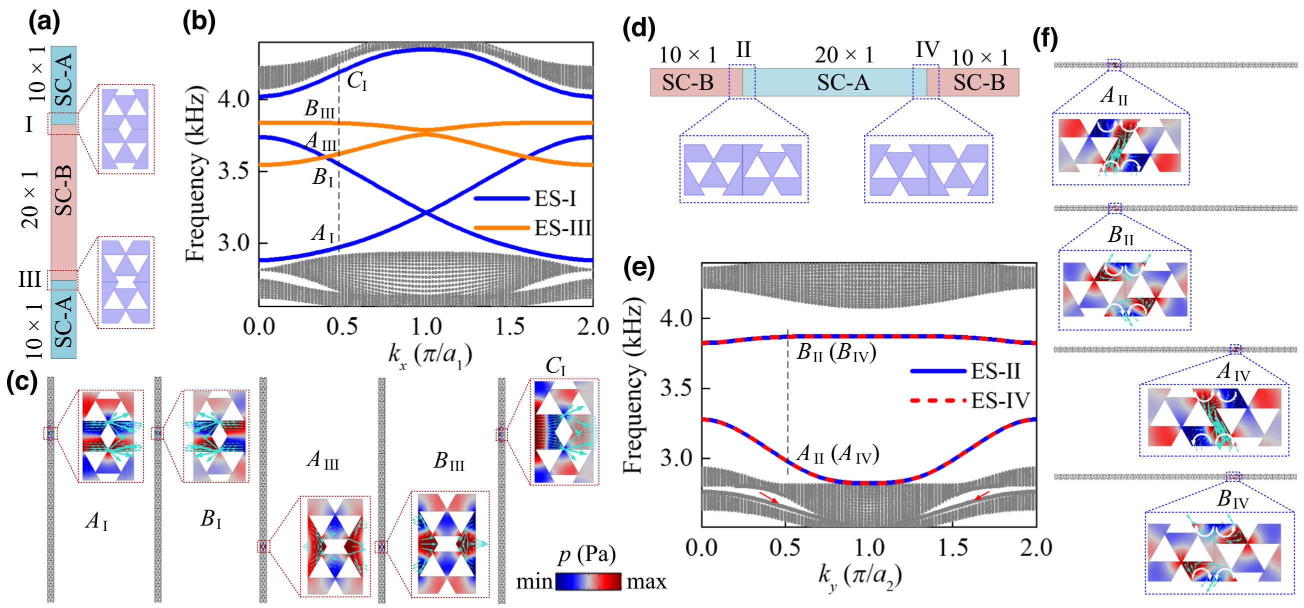

FIG. 4. (a) Scheme of the superlattice composed of SC-A and SC-B with interface I and interface III. Red dotted rectangular box depicts a magnified view of interfaces I and III. (b) Acoustic band structure of the supercell (a) around the quasi-type-II DP. Black dots represent bulk bands. Blue and orange lines represent the edge states located on interfaces I and III, respectively. (c) Acoustic pressure patterns and energy flow of eigenmodes A_I, B_I, and C_I at interface I, and A_III and B_III at interface III at $k_x = 0.5$. (d) Scheme of the superlattices obtained by combining SC-A and SC-B. Their respective interfaces are denominated as interface II and interface IV. Blue dotted rectangles show magnified views of the two interfaces. (e) Band structure the supercell containing interfaces II and IV, where the dotted lines represent bulk modes. Blue lines (ES-II) and red dashed lines (ES-IV) represent the edge states located at interface II and interface IV, respectively. (f) Pressure patterns and energy-flow distribution of the eigenstates denominated A_II, B_II, $A_\mathrm{IV,}$ and B_IV. Colored maps represent the acoustic pressure (real part), and cyan arrows represent the energy flux.

overlapping bulk bands (black dots) near the degeneracy point. The quasi-type-II DP in the ASP is analogous to the valley edge state, since it originates from the Dirac point of the triangular lattice, which sustains time-reversal symmetry. Therefore, the band structure is symmetric with respect to $k_x = 1$. In addition, as shown in Fig. 4(b), there are forward-moving states, with group velocity $d\omega/dk > 0$, and backward-moving states with group velocity $d\omega/dk < 0$ [55]. Due to the strong perturbation of the sound field by the irregular structure on interface III, a narrow band gap occurs between the forward- and backward-propagating edge states. The underlying physics of the edge-state band is related to the energy vortex [36]. For the acoustic valley Hall effect realized by the triangular lattice, the zigzag-type interface is actually composed of the discrete centers of the triangular lattice, and there is only one vortex at the center of the triangular lattice, and the vortex directions of the two inequivalent lattice centers are different [35,36,54]. Therefore, there are usually two bands of edge states on the interface formed by two phononic crystals with distinct topological phases [35]. However, due to the diversified vortex information, as shown in Fig. 3(c), there are three bands of the edge states. The edge states located on the interfaces are the result of hybridization of the eigenmodes of the cells on both sides of the interface, thus presenting rich edge-state information [29].

Figure 4(c) shows the sound-pressure patterns and sound-field-intensity distribution of eigenmodes A_I, B_I, and C_I at interface I, and A_III and B_III at interface III calculated at $k_x = 0.5$. The patterns of eigenmodes A_I, B_I, and C_I show localization on interface I, and A_III and B_III are located at interface III (magnified views are shown in the red dotted rectangle) and correspond to topologically protected edge states. In addition, the intensity distribution, indicated by the cyan arrows, shows the direction of motion of the edge states corresponding to the forward- and backward-moving states. However, as shown in Fig. 4(c), the group velocity of B_III is almost zero (flat band) and its direction of propagation is not obvious.

Figure 4(d) depicts the horizontal supercell containing interfaces II and IV, which is the same size as a vertical supercell. The projected band structure of the horizontal supercell is plotted in Fig. 4(e), where the blue lines (ES-II) and red dashed lines (ES-IV) within the band gap of the bulk indicate the edge states on interfaces II and IV, respectively. At $k_y = 0.5$, we select four edge states denominated by A_II, B_II, A_IV, and B_IV, in which the subscripts II and IV represent interfaces II and IV, respectively. Figure 4(f) shows the distribution of acoustic pressure localized near interface II and interface IV. The white circular arrow indicates the propagation direction of the acoustic energy flow. Since the two SCs do not form any new geometric shapes at the interfaces, the pressure pattern at the interface is directly related to that of the eigenmodes in the unit cell. For example, the A_{II} mode in Fig. 4(f) can be obtained by just joining the patterns of modes D_2 and D_4 represented in Fig. 3(c). Similarly, mode B_{II} in Fig. 4(f) can also be obtained by sequentially joining the two higher-frequency modes represented in Fig. 3(c). For modes A_{IV} and B_{IV}, the cases are the same as those of A_{II} and B_{II}. This is the reason that the band structure for interfaces II and IV are the same. Within the bulk band, there is also a band [indicated by the red arrows in Fig. 4(e)] composed of edge states near 2.6 kHz. The projected bands are composed of tilted type-II valley Hall kink states [28,43], due to the type-II DP (D-II) in Fig. 1(b).

C. Directionality of topological edge states

The pressure patterns of edge states at the four interfaces are confined near the interface, and they have recognizable symmetries, especially at interfaces I and III. To understand the influence of symmetry on the transport properties of sound waves, we study the structure shown in Fig. 5(a), where the four quadrants are made of different unit cells. A Cartesian coordinate system is added at the center of this structure, which is divided into four equal parts, 1–4, in which the upper region (the part composed of regions "1" and "2") and the lower region (the part composed of regions "3" and "4") represent different SCs. For the convenience of description, bands ES-I, ES-II, ES-III, and ES-IV composed of edge states are divided. ES-I, for example, is divided into ES-I-1 and ES-I-2, where the frequency in ES-I-1 is lower than that in ES-I-2. Besides, we define a symmetry rule as follows: when the mode pressure

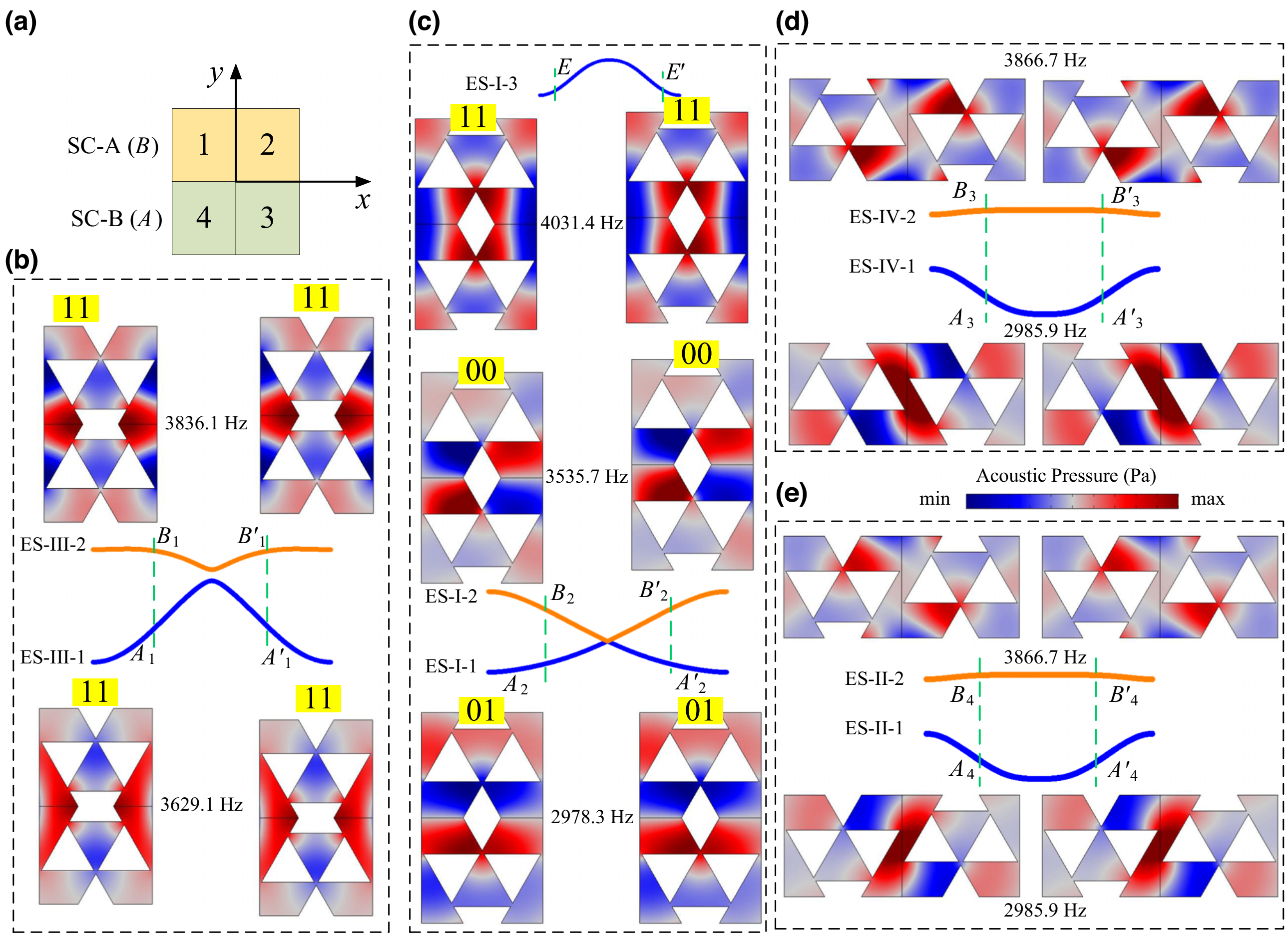

FIG. 5. (a) Scheme of the structure containing SC-A and SC-B. SC is divided into four regions, 1–4, where four different interfaces can be formed. (b) Snapshots of the sound-pressure pattern of the edge states located at interface III (calculated at $k_x = 0.5$ and 1.5). Numbers highlighted in yellow represent the mirror symmetry about the x-z plane and y-z plane, 1 means symmetric and 0 means antisymmetric. Blue and orange lines provide the dispersion relation of the edge modes. (c) Snapshots of the sound-pressure pattern of the edge state located along interface I. Upper panel corresponds to eigenmodes at $k_x = 0.1$ and 1.9, and the middle and lower panels represent eigenmodes at $k_x = 0.5$ and 1.5. (d),(e) Sound-pressure patterns of edge states at interfaces IV and II, respectively. Color scale represents the magnitude of the real component of pressure, going from negative values (blue) to positive values (red).

map is symmetric about the coordinate axis, it is marked as "1," and when it is antisymmetric about the coordinate axis, it is marked as "0." Therefore, two digits can express the symmetry of the SC structure. The first digit indicates symmetry about the x axis, while the second digit indicates symmetry about the y axis. First, let us analyze the case where the upper region is SC-B, as shown in Fig. 5(b). On the bands of the edge states (indicated by blue and orange solid lines in the figure), we select four edge modes (at $k_x = 0.5$ and $k_x = 1.5$): A_1, B_1, A_1', and B_1'. Their pressure maps have the same symmetry, indicating that all have symmetry "11," highlighted in yellow.

When the upper region is changed to SC-A, the symmetry becomes complicated due to the number of bands containing edge states. As shown in Fig. 5(c), the upper panels depict the high-frequency boundary states E and E', obtained at wave vectors $k_x = 0.1$ and 0.9, respectively. Their pressure patterns indicate that their symmetry is also "11." While for edge states with lower frequency, as shown in the middle and lower panels of Fig. 5(c), calculated at $k_x = 0.5$ (1.5), the symmetry of the modes A_2 (A_2') and B_2 (B_2') about the x axis becomes antisymmetric and they should be labeled with "0." Therefore, the symmetries of A_2 (A_2') and B_2 (B_2') can be labeled "01" ("01") and "00" ("00"), respectively. Figures 5(d) and 5(e) represent the two kinds of horizontal structures, where the patterns can no longer be labeled with integers due to their lack of symmetry about the x or y axis. However, they exhibit obvious directivity that could be defined by a fractional number.

The realization of topological edge states in the acoustic Suzuki phase requires two key factors, the double-degenerate point and the crystals on both sides of the domain wall with equal magnitudes of Berry curvature but opposite signs, which are also the prerequisites for valley edge states [35,56,57]. And this is the main reason that the topological edge states in the ASP are regarded as valleylike edge states. However, different from the previous valley edge states, in the ASP, the degenerate point is not caused by lattice symmetry [36,57], but by the mechanism of generalized band folding, and it appears at the low-symmetry point in the FBZ instead of the corners [35,56,57]. The projected band structure of the vertical and horizontal supercells shows that the topological edge states can appear on four boundaries of the unit cell, and the frequencies and number of edge states are different because of geometric configurations at the domain walls. Due to the modulation of the scatterer shape, the edge states stem from the quasi-type-II DP in the ASP and display obvious symmetry about the directional axis, such as the x axis, y axis, or one specified axis; these are different from the chiral edge states of the acoustic quantum Hall effect [19,58], the valley-vortex edge states of the acoustic valley Hall effect [35,36], and the helical edge states in the acoustic quantum spin Hall effect [37,38]. As a consequence, excitation of the edge modes strongly depends on the symmetry of the wave employed as the excitation source, as observed for acoustic modes in a typical SC [59]. From the pressure pattern of the modes depicted in Fig. 5, the edge states with the lowest frequencies at interface I (A_2, A_2', B_2, and B_2') are particularly interesting, since they are antisymmetric with respect to the x-z plane. Therefore, for an incident plane wave traveling along the x axis, these edge states cannot be excited by such an excitation source [59]. These edge states are said to belong to a deaf band of edge states, a phenomenon that is reported here in relation to acoustic topological states. As for eigenstates in other interfaces, they can be excited by an incident plane wave along the x axis because their pressure pattern has mirror symmetry for the x-z plane. For a comprehensive study regarding the conditions, in terms of symmetries, for the excitation of edge states by external excitation sources, see Appendix E.

D. Acoustic Shannon entropy of topological edge states

The acoustic Shannon entropy (ASE) is a useful tool to characterize the spreading of acoustic eigenmodes. It was introduced by Sánchez-Dehesa and Arias-Gonzalez [60] as $S_u = -\int P(\mathbf{r}) \ln P(\mathbf{r}) d\mathbf{r}$, where $P(\mathbf{r})$ represents a false probability distribution function defined as $P(\mathbf{r}) = A|u(\mathbf{r})|^2 / \int |u(\mathbf{r})|^2 d\mathbf{r}$; $|u(\mathbf{r})|^2$ is the square norm of the total acoustic pressure and A is the area of the integration domain. The ASE is then a quantity providing information to measure the spatial localization of a given acoustic mode, and it increases with increasing uncertainty (i.e., spreading of the mode).

Figure 6 shows the calculated ASE corresponding to bands ES-I, ES-II, ES-III, and ES-IV. In Fig. 6(a), green, blue, and orange lines represent topologically edge states ES-I-1, ES-I-2, and ES-I-3, respectively. The localization degree of the edge states is different and depends on the k wave number. For example, the spreading of edge states belonging to ES-I-2 is smaller than the other two. Figure 6(b) shows the ASE distribution of the eigenmodes of the supercell including interface III, in which the localization degree of topological states on ES-III-1 (green line) is higher (with a lower value of ASE) than that on ES-III-2 (blue line). The lines for the eigenmodes in ES-II(IV)-1 (green line) and ES-II(IV)-2 (blue line) are crossing, and the ASE for ES-II(IV)-2 has a slight change in the interval $0.4 < k < 1.6$, as shown in Fig. 6(c). The greater the Shannon entropy is, the larger the spreading of the acoustic mode [60]; hence, the corresponding propagation is different. The one-dimensional (1D) projection spaces of the vertical and horizontal supercells are shown in Fig. 6(d), and the projection vector space of the vertical and horizontal supercells are the k_x and k_y directions, respectively. According to the projected band structure and ASE of the edge states, when additional structures appear on the interface, the topological states are not only related to the

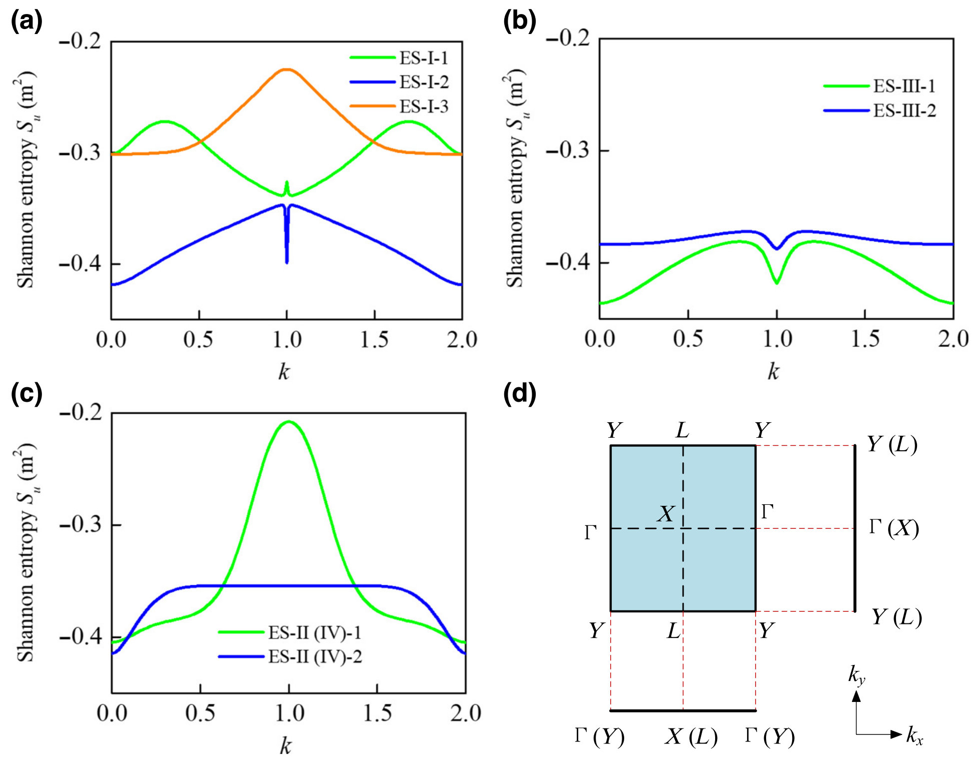

FIG. 6. (a) Acoustic Shannon entropy of eigenmodes localized at interface I. Green, blue, and orange lines represent topologically protected edge states ES-I-1, ES-I-2, and ES-I-3, respectively. (b) Acoustic Shannon entropy corresponding to eigenmodes localized at interface III. Green and blue lines represent edge states ES-III-1 and ES-III-2, respectively. (c) Acoustic Shannon entropy corresponding to eigenmodes localized at interface II(IV). Green and blue lines represent edge states ES-II(IV)-1 and ES-II(IV)-2, respectively (d) 1D projection of the vector of the 2D first BZ of the Suzuki phase in the k_x and k_y directions.

interface of the supercell, but also to the type of supercell (the direction of the projected space).

E. Transport along domain walls

The paramount property of topological nontrivial systems is the exhibition of unidirectional and robust propagation with edge states existing at the interfaces between distinct topological zones. As described above, the symmetry of the pressure patterns of the edge states enrich the transmission features through topological edge modes. On the other hand, some asymmetric scattering, producing an effective component perpendicular to the incident-wave vector, can easily modify the incident exciting plane wave. Therefore, when 2D plane waves impinge on the structure through the four different interfaces, a variety of transmission behaviors appear, depending on the incident directions. Figure 7(a) shows a diagram that condenses the information regarding the bandwidths of topological edge states in vertical and horizontal supercells. In this diagram, the blue and red stripes in the first row represent the bands containing edge modes localized on interface I (schematically depicted at the right-hand side), while the edge modes localized on interface III (schematically depicted at the right-hand side) are represented by the green and orange stripes in the second row. Finally, cyan and purple stripes in the last row define the frequency range containing edge modes along interfaces II and IV (interface IV is schematically depicted on the right-hand side). Since some bands have overlapping frequency regions, the edge states in these regions can perform multichannel wave transmission, a property with interesting engineering applications. To study the topological transmission, the diagram is further divided into seven frequency bands, named EG-A, EG-B, EG-C, EG-D, EG-E, EG-F, and EG-G, as shown in Fig. 7(a). The values define the frequencies of the seven bands. It should be noted that the frequencies reported here correspond to states in the bulk band gap, which is slightly different from that of the total dispersion relation.

Figure 7(b) shows the scheme of the composite SC structure employed to study the different possibilities of topological wave transport. They can be obtained because of the frequency and symmetry features of topological edge modes. The structure composed of two SC-A (blue areas) and two SC-B (orange areas) is made of 16×16 cells and contains the four interfaces I–IV. Thick red lines, with length a, represent the incident planes, the centers of which are at the interfaces. In the numerical simulations,

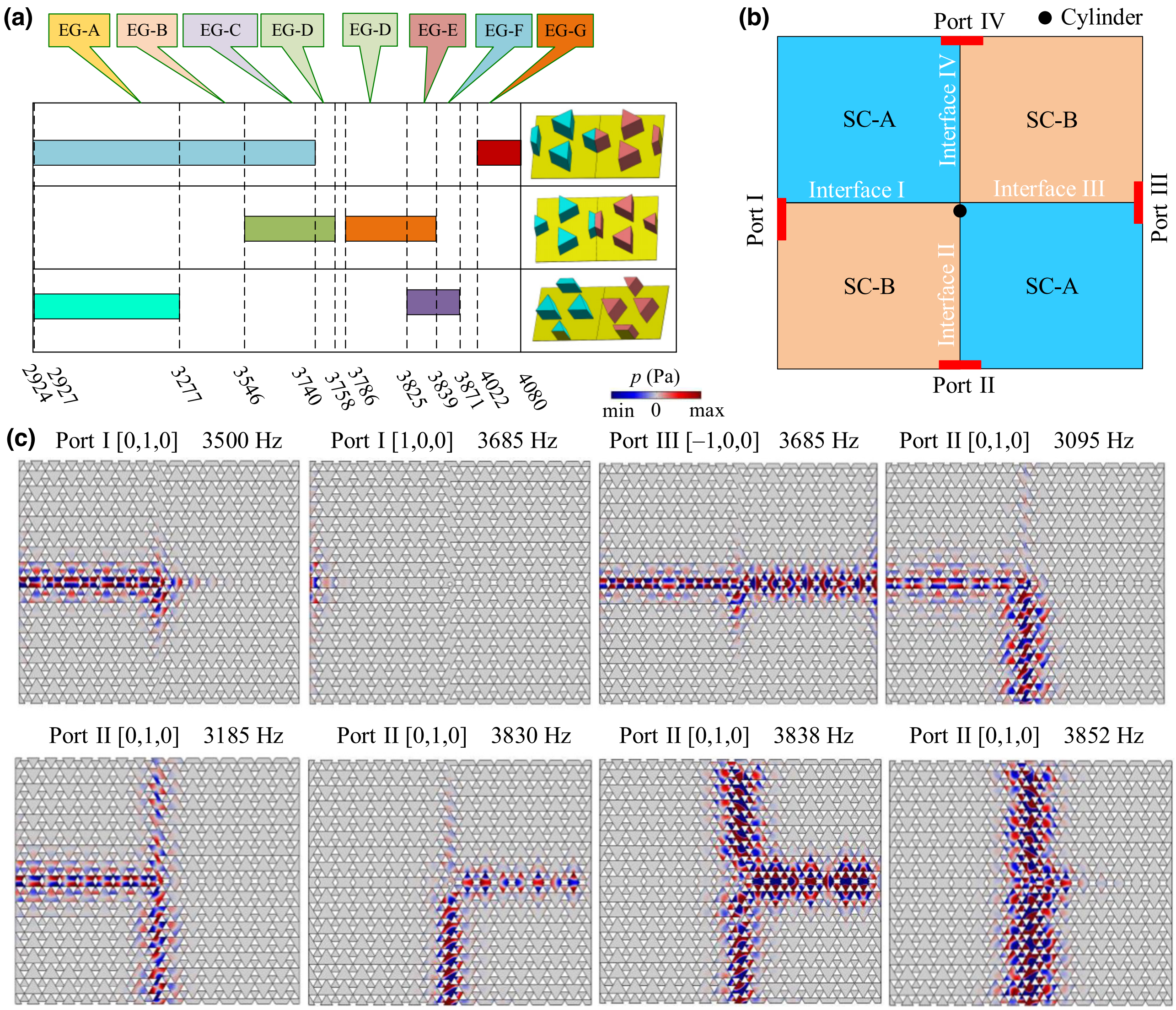

FIG. 7. (a) Frequency spectra of the topologically protected edge states. First row indicates the frequencies of states (blue and red stripes) of supercell containing interface I. Second row defines frequencies (green and orange stripes) with states localized at interface III. Cyan and magenta stripes in the third row indicate the frequencies of edge states localized at interface II or IV. Bands are further divided into seven smaller frequency bands (defined on top) according to overlapping features. (b) Scheme of a SC structure made of SC-A and SC-B containing four interfaces. Distinct edge states are excited through ports named I, II, III, and IV. Black dot indicates the auxiliary cylinder employed to disturb the field of the impinging waves arriving at the ports. (c) Propagation of a plane wave with direction [0, 1, 0] at 3500 Hz from port I, with direction [1, 0, 0] at 3685 Hz from port I, with direction [−1, 0, 0] at 3685 Hz from port III, with direction [0, 1, 0] at 3095 Hz from port II, with direction [0, 1, 0] at 3185 Hz from port II, with direction [0, 1, 0] at 3830 Hz from port II, with direction [0, 1, 0] at 3838 Hz from port II, and with direction [0, 1, 0] at 3852 Hz from port II.

a perfect matching layer is applied around the boundaries of the structure. In addition, we introduce a defect cylinder (see the black dot around the center of the structure) that can be ignored due to the topology, but it can create additional modes. Next, we apply plane waves impinging on the different ports to analyze the transmission characteristics in the combined structure, with frequencies within the overlapping bands, EG-A, EG-C, and EG-E, and the single band, EG-F (see Appendix F).

Due to the overlap of the bands of topological edge states localized on different interfaces in the ASP, backscattering-suppressed sound propagation can be achieved in the channels composed of different interfaces (see Appendix F). Combined with the symmetry and locality of the edge-state eigenmodes, the sound wave exhibits extraordinary properties in the ASP, as shown in Fig. 7(c). For example, when the plane wave with direction [0,1,0] at 3500 Hz impinges on port I, sound waves can only be localized on the incident interface I, and this feature can be used to identify the existing source. In the EG-C band, when the plane wave with direction [1,0,0] at 3685 Hz impinges on port I, the transmission is forbidden because the symmetry of the edge states is orthogonal to that of the exiting wave. However, when the plane wave with the same frequency in direction [−1,0,0] impinges on port III, the edge modes along interfaces III and II can be excited because they have the same symmetry. This property can be exploited to realize acoustic transmission with nonreciprocal properties, namely, acoustic diodes. In addition, multichannel wave transport is also possible, i.e., when the waves enter one port and are transmitted to more than one port at the output. However, based on the Shannon entropy, let us point out that the sound energy transmitted along the multichannel is not equally distributed, so the sound energy in the other exit port could be almost zero, as shown in Fig. 7(c) with wave direction [0, 1, 0] at 3095, 3185, 3830, 3838, and 3852 Hz from port II. In summary, the transmission properties show that ASP crystals can be employed to develop acoustic devices like acoustic diodes, multichannel and selective acoustic transmission, and sound-source recognition.

IV. STUDY OF TOPOLOGICAL STATE TRANSPORT

For horizontal supercells, the topological eigenmodes located in the bulk band gap do not have mirror symmetry about the X-Z plane or Y-Z plane (see Fig. 5) and, therefore, they are insensitive to the direction of the incident wave. In addition, compared with the vertical supercells, the values of the ASE of the horizontal supercells are larger, meaning a wider spreading of their eigenmodes. Therefore, to study the propagation properties under a given incident direction, we consider the experimental characterization of the horizontal supercell and assume that similar results would be obtained for the vertical supercells.

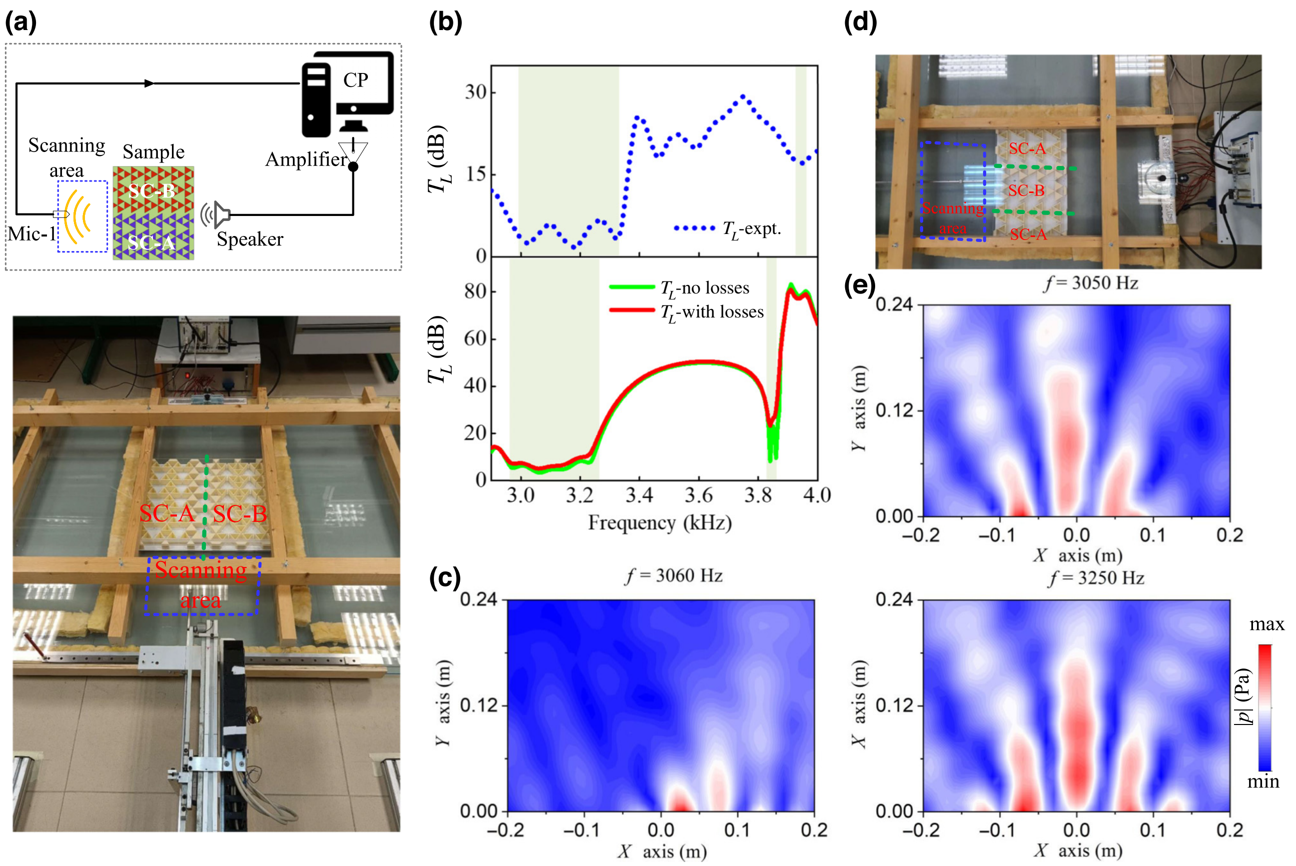

FIG. 8. (a) Experimental setup. Top panel and bottom panel show a scheme and photograph of the data acquisition process, respectively. (b) Transmission loss (T_L) calculated (bottom panel) and measured (upper panel). Red and green lines define the T_L obtained with and without thermoviscous losses, respectively. Blue dotted line represents the T_L obtained from measurements. Shaded areas define the bandwidth of the edge states. (c) Absolute pressure pattern at the scanning area was obtained experimentally. (d) Experimental setup for acoustic focusing. (e) Absolute pressure distribution in the scanning area obtained experimentally at 3050 Hz (top panel) and 3250 Hz (bottom panel). Color represents the absolute pressure.

Figure 8(a) shows the experiment setup (see Appendix H), in which the size of the sample made of SC-A and SC-B containing 6×6 cells. As a comparison, we designed a structure with the same size for simulation calculations. To quantify the amount of sound transmission, we use the transmission loss (T_L), which is defined as $T_L = 10\log(P_{\text{in}}/P_{\text{out}})$. Here, P_{in} and P_{out} represent the acoustic energy density at the entrance and exit of the sound field, respectively. The sound energy density can be calculated by (see Appendix H) $P_{\text{in}} = \int p_0^2/2\rho_{\text{air}}c_{\text{air}}$ and $P_{\text{out}} = \int |p|/2\rho_{\text{air}}c_{\text{air}}$. As shown in Fig. 8(b), the red (green) line represents the simulated T_L with (without) thermoviscous losses taken into account, while the blue dotted line represents the T_L obtained from measurements. The shaded areas in both panels represent the bandwidths of the topological edge states. The numerical simulations indicate that thermoviscous effects are not relevant. However, the comparison with the experimental T_L indicates that the measured T_L profile is blueshifted, and the bandwidth of the lower band has also increased with respect to that theoretically calculated. The origin of such disagreement is the small discrepancy in the size of the manufactured rods (see Appendix G for details). In addition, notice that the TL of modes belonging to the second band is larger than that of the first band, since the dispersion relation is almost flat and, consequently, the thermoviscous losses are enhanced due to the extremely low group velocity. Moreover, the higher value of the ASE, indicating a large spreading of the mode, also contributes to the increase of the TL.

In addition, Fig. 8(c) shows the measurements of the absolute pressure taken at 3060 Hz, as an example, in an area at the output of the interface. This 2D map indicates that sound propagation has obvious directivity when the waves exit the interface. The underlying physical mechanism of this directional propagation is the symmetry of the eigenmodes of the edge states, and the pressure field is modulated by the eigenmodes when the plane wave incident on the structure excites the eigenmodes at the interface, thus producing directional propagation. This directional effect inspired us to achieve acoustic focusing by using two topologically protected edge states obtained in nearby interfaces. Since interfaces II and IV have the same dispersion relationship, we have designed a sandwich structure composed of SC-A and SC-B with 4×6 cells, as shown in Fig. 8(d), which describes the experimental setup. After the wave emits along interfaces II and IV, due to the directionality of the wave, the wave front of the outgoing wave at the two ports forms a stable crossing area, also called energy convergence, showing the characteristics of acoustic focusing. The measurements shown in Fig. 8(e) illustrate this property at two different frequencies, where the output beams with principal directions $\pm 30°$ interfere in the area in front of the sample. For further details about directivity propagation, see Appendix I.

V. CONCLUSIONS

To summarize, this work demonstrates the unique properties exhibited by topological states related to quasi-type-II DPs in the acoustic-Suzuki-phase crystal. Particularly, they are different from the chiral edge states in the acoustic quantum Hall effect, the valley-vortex edge states in the acoustic valley Hall effect, and the spiral edge states in the acoustic quantum spin Hall effect; the edge states in the ASP are characterized by symmetry and directionality. The rich information acquired on topological states in the ASP can be harnessed to achieve interesting acoustic functionalities. For instance, using states belonging to deaf bands to create an acoustic diode, employing Shannon entropy for multichannel and selective sound transmission, and exploiting directionality to produce acoustic focusing. These features open alternative paths for the design of highly integrated multifunctional acoustic devices. Let us note that our results in acoustics can be extended to other classical waves, such as electromagnetic and elastic waves, which can further enrich the study of topological states.

ACKNOWLEDGMENTS

Work supported by the RDI Grant No. PID2020-112759GB-I00 funded by MCIN/AEI/10.13039/501100011033. Z.H. acknowledges a scholarship with Grant No. 202206280162 provided by the China Scholarship Council. The group at Xi'an Jiaotong University acknowledges the support of the National Natural Science Foundation of China under Grant No. 52250287.

APPENDIX A: NUMERICAL SIMULATIONS

The numerical simulations are performed using the commercial software COMSOL Multiphysics, which is based on the finite-element method. We employ the "pressure acoustic module" to visualize the modal characteristics and propagating features of acoustic waves. The materials involved in the simulations are air (the background material) and acrylonitrile butadiene styrene (ABS), which is employed in manufacturing the scatterers. The mass density and velocity of air are $\rho_{\text{air}} = 1.25$ kg/m^3 and $c_{\text{air}} = 343$ m/s, respectively. The physical parameters for ABS are $\rho_{\text{ABS}} = 1060$ kg/m^3 and $c_{\text{ABS}} = 2400$ m/s. Due to the large mismatch between the acoustic impedances of air and ABS, in the calculations, we consider that the scatterer acts as a rigid body. The mesh type is free triangular, and the largest mesh-element size is lower than 1/15th of the shortest incident wavelength. In the band-structure calculations, Floquet conditions are imposed on the boundaries of the unit cell. For the simulation of wave transmission, the sound source of the structure adopts the background pressure field with a width of $4a$. Perfectly matching layers are imposed around the structure. When calculating the transmission loss, the integral path for the entrance is the boundary between the background-pressure field and the structure. The integral path at the exit is parallel to the path of the entrance with the same length $4a$, which is located 0.5 mm outside the structure. To analyze the effects of viscous and thermal losses caused by scatterers in the structure, we applied the "thermoviscous acoustics, frequency domain" interface. During the thermoviscous simulation calculation process, the viscous-boundary-layer thickness is defined at the maximum value under study. The viscous-boundary-layer thickness, $\varepsilon_{\text{visc}}$, is set by $\varepsilon_{\text{visc}} = \sqrt{2\mu/(\omega\rho_0)}$, where μ and ω are the dynamic viscosity and angular frequency, respectively.

APPENDIX B: DIRAC POINTS IN THE SUZUKI PHASE AND TRIANGULAR LATTICE

It is exciting to discover the double-degenerate point in the ASP lattice, since double degeneracy is the paramount condition for realizing the topological edge states in acoustic valleys. However, different from the type-I DP at the corners of the FBZ, due to crystal symmetry [36], the accidental DP formed by the fourth and fifth bands in the ASP is located at the low-symmetry point in the FBZ, and the cone related to the DP lacks obvious tilted features in a specific direction [28,43]. Therefore, it can be denominated as a quasi-type-II DP. Next, we analyze the reasons explaining the occurrence of the quasi-type-II DP. As shown in Fig. 9(a), the sonic crystal under study can be regarded as a rectangular lattice of vacancies created in the well-known triangular lattice. The blue dotted hexagon represents the unit cell of the triangular lattice with primitive vectors $\mathbf{A}_1$ and $\mathbf{A}_2$ and $|\mathbf{A}_1| = |\mathbf{A}_2| = a$. Thus, the complete crystal can be obtained by repetition of the unit cell (containing a single scatterer) at the lattice positions generated from $\mathbf{A}_1$ and $\mathbf{A}_2$. However, the triangular lattice can also be generated using primitive vectors $\mathbf{a}_1$ and $\mathbf{a}_2$, previously used to describe the ASP. The unit cell of the ASP, represented by a blue dotted rectangular box, contains three scatterers instead of four, since the red triangles represent the vacancies created in the original triangular lattice. When $a = 50$ mm and $R = 0.45a$, the band structure of the ASP is shown in Fig. 9(b), where I_1 defines the position between the fourth and fifth bands where the quasi-type-II DP appears. The inset represents the unit cell that is repeated at the lattice position generated by $\mathbf{a}_1$ and $\mathbf{a}_2$. For the sake of comparison, Figs. 9(c) and 9(d) show the frequency-band structures of the crystal cell represented by the blue dashed

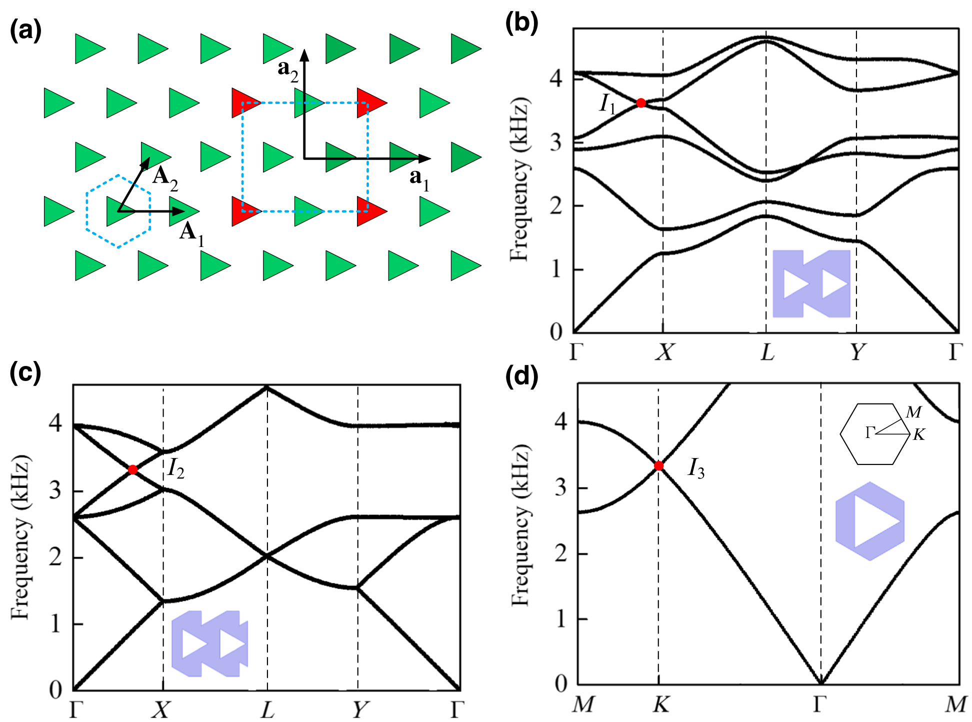

FIG. 9. (a) Schematic diagram of a sonic crystal consisting of scatterers with a triangular section distributed in a triangular lattice. Blue dashed hexagon represents the primitive unit cell of the triangular lattice defined by vectors $\mathbf{A}_1$ and $\mathbf{A}_2$. Rectangle represents the unit cell of the ASP in which the unit cell contains three scatterers. Red triangles represent the vacancies created in the triangular lattice. (b) Acoustic band structure of the ASP. Inset shows the unit cell of the ASP. DP is denominated as I_1. (c) Dispersion structure of the lattice represented by the blue dotted rectangular box in (a). Fourth and fifth bands appear as Dirac cone point I_2 in the Γ-X direction. Inset represents the cell structure. (d) Band structure of the triangular lattice obtained with the unit cell shown in the inset. Type-I Dirac point I_3 appears at corner point K.

rectangle and the unit cell represented by the blue dashed hexagon, respectively. Note that the frequency positions, I_2 and I_3, appear at the same frequency in both figures. In fact, due to the scatterer displaying C_{3v} symmetry consistent with the triangular lattice, I_3, which is located at the corner of the FBZ, is a type-I Dirac point [21]. For the triangular lattice, the frequencies of points I_3 in the band structure of the unit cell containing one scatterer and I_2 in the band structure of the cell containing four scatterers are the same. Although the frequencies of points I_1 and I_2 are different, the band structure of the Suzuki phase is like that of the triangular lattice described with four scatterers in the unit cell, which indicates that there should be a connection between the three double-degenerate points I_1, I_2, and I_3.

APPENDIX C: BERRY CURVATURE IN THE ACOUSTIC SUZUKI PHASE

Topological phase transitions are one of the most important highlights of recent condensed-matter physics. In the frequency-band structure, for an acoustic system with energy valleys due to band degeneracy, an important method to measure the topological nontrivial phase is to calculate the valley Chern number. The Chern number can be obtained by integrating the Berry curvature, $\mathbf{F}_n(\mathbf{k})$, over the wave vector $\mathbf{k}$ space in a 2D torus [49]. For example, for the nth band in the band structure, the formula to calculate its Chern number, C_n, in the continuous space is defined as [50,51]

$$C_n = \frac{1}{2\pi}\iint \mathbf{F}_n(\mathbf{k})d^2\mathbf{k}. \tag{C1}$$

To simplify the calculation, the result of the Chern number can be obtained on a discretized Brillouin zone [50]. Here, we use the general approach, which discretizes the two boundary vectors, k_{j_s} ($s = 1, 2$), of the first Brillouin zone with a rectangle shape into N_1 and N_2 points, respectively. Then in the 2D vector space, the coordinates of any point are denoted as

$$k_b = (k_{j_1}, k_{j_2}) \quad (b = 1, 2, \ldots, N_1N_2), \tag{C2}$$

where

$$k_{j_s} = \frac{2\pi}{a_s} \times \frac{j_s}{N_s}\ (j_s = 0, 1, \ldots, N_s - 1).$$

Setting $N_s = a_\mu N_B$ ($s \neq \mu$), in this way, the unit piece is a square with the size $2\pi/(a_1a_2N_B)$. For each discrete unit piece with area ΔS_k, the integral value of Berry curvature on it is

$$\mathbf{F}_n(\mathbf{k})\Delta S_k = \frac{1}{2\pi}\mathrm{Im}(\ln[U_{k_1\to k_2}(k_b)U_{k_2\to k_3}(k_b) \times U_{k_3\to k_4}(k_b)U_{k_4\to k_1}(k_b)]. \tag{C3}$$

Here, $U_{k_h\to k_g}(k_b) = \left|\left\langle \Psi_{n,k_{j_h}}(k_b)|\Psi_{n,k_{j_g}}(k_b)\right\rangle\right|$, where h, $g = 1, 2, 3, 4$, and the inner product in the formula can be defined as

$$\left\langle \Psi_{n,k_{j_h}}(k_b)|\Psi_{n,k_{j_g}}(k_b)\right\rangle = \iint \Psi^*_{n,k_{j_h}}(\mathbf{r})\cdot\hat{\mathcal{B}}(\mathbf{r})\cdot\Psi_{n,k_{j_g}}(\mathbf{r})dS, \tag{C4}$$

where $\Psi_{n,\mathbf{k}}(\mathbf{r})$ is the $\mathbf{k}$-dependent wave function of the nth band in the acoustic wave; $\hat{\mathcal{B}}(\boldsymbol{r})$ is the energy density operator, and its function is to make the integral on the right side of Eq. (C4) proportional to the energy of the sound wave when $\mathbf{k} = \mathbf{k}'$. For acoustic waves, the energy density operator is

$$\hat{\mathcal{B}}(\mathbf{r}) = \frac{1}{2\rho(\mathbf{r})c(\mathbf{r})^2}, \tag{C5}$$

where ρ is the mass density and c is the speed of sound. Both the density and speed depend on the medium at position $\mathbf{r}$ [49].

Note that, for an acoustic Bloch wave function, $\Psi_{n,\mathbf{k}}(\mathbf{r}) = e^{i\mathbf{k}r}p_{n,\mathbf{k}}(\mathbf{r})$, during the calculation, the periodic part of the Bloch function, $p_{n,\mathbf{k}}(\mathbf{r})$, which gives the acoustic pressure distribution for the nth acoustic band with wave vector $\mathbf{k}$, needs to be normalized. The formula is defined as [49]

$$\mathcal{A}_{n,\mathbf{k}} = \iint p^*_{n,\mathbf{k}}(\mathbf{r})\cdot\frac{1}{2\rho(\mathbf{r})c(\mathbf{r})^2}\cdot p_{n,\mathbf{k}}(\mathbf{r})dS. \tag{C6}$$

Therefore, a new inner-product expression needs to be defined on the basis of Eq. (C4), as follows:

$$\left\langle \Psi_{n,k_{j_h}}(k_b)|\Psi_{n,k_{j_g}}(k_b)\right\rangle = (\mathcal{A}_{n,\,k_{j_h}}\mathcal{A}_{n,\,k_{j_g}})^{-1/2}\iint \Psi^*_{n,k_{j_h}}(\mathbf{r})\cdot\hat{\mathcal{B}}(\mathbf{r})\cdot\Psi_{n,k_{j_g}}(\mathbf{r})dS. \tag{C7}$$

The integral of the Berry curvature on each discrete unit block can be obtained from Eqs. (C3) and (C7). Then, the Chern number of Eq. (C1) can be calculated by adding up the integral values on all discrete unit pieces, and the expression is given by

$$C_n = \sum_{b=1}^{N_1N_2}\mathbf{F}_n(\mathbf{k})\Delta S_k. \tag{C8}$$

According to Eq. (C8), based on the distribution of $\mathbf{F}_n(\mathbf{k})\Delta S_k$ in parameter space, that is, the Berry curvature, the topological properties of the energy band can also be characterized. The results are plotted in Figs. 4(e) and 4(f).

APPENDIX D: BAND STRUCTURE OF A TRIVIAL TOPOLOGICAL INSULATOR

In the process of scatterer rotation, the SCs before and after degeneration of DPs have different topological phases, and there are topologically protected edge states of the interface composed of two SCs with distinct topological phases [35]. While there are no edge states on the interface separating two SCs with the same topological phase. As shown in Fig. 10(a), from the band structure of the ASP with rotation angles of $\beta = 25°$ (blue vertical short line) and $\beta = 35°$ (red horizontal short line), the two cases are nearly the same. At $k = 0.6695$, eigenstates $M1$ and $M2$ are taken from the fourth and fifth bands of a SC with $\beta = 35°$ (SC-C), and $M3$ and $M4$ from the fourth and fifth bands of a SC with $\beta = 25°$ (SC-D). Figure 10(b) depicts the pressure patterns of these four eigenmodes, showing that the modes of the two SCs are the same, and therefore, the two SCs have the same topological phases.

Figure 10(c) schematically depicts a vertical supercell containing interface T-I composed of SC-C (upper) and SC-D (lower), and interface T-II composed of SC-C (lower) and SC-D (upper). The supercell contains 40×1 cells, of which both ends contain 10×1 cells. The red dashed rectangle shows magnified views of the two interfaces. Figure 10(d) shows the projected band structure of the vertical supercell, in which there are no edge states within the overlapping bulk band gap. Moreover, the same situation exists in the projected bands [Fig. 10(f)] of the horizontal supercell [Fig. 10(e)]. It is observed in Fig. 10 that there are no topological edge states on the interface composed of SCs with the same topological phase.

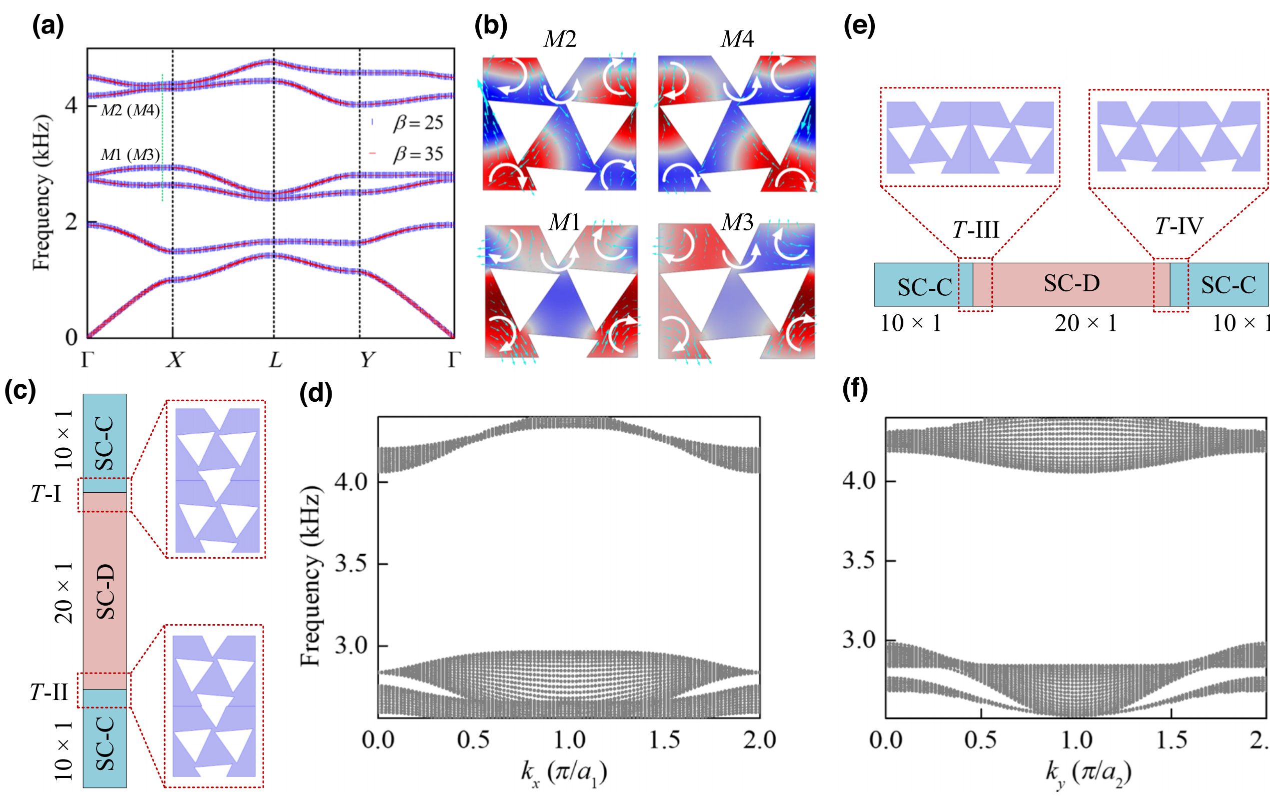

FIG. 10. (a) Band structure with different rotation angles. Blue vertical short line and red horizontal short line represent the band structure when $\beta = 25°$ and $\beta = 35°$, respectively. Green dotted line indicates $k = 0.6695$, and the intersection of SC with the fourth and fifth bands at an angle of rotation of 25° (35°) is indicated by $M1$ ($M3$) and $M2$ ($M4$). (b) Sound-pressure mode of states $M1$–$M4$. Color represents the sound pressure (real part), in which red and blue colors represent positive and negative values, respectively. Cyan arrow indicates sound intensity, and the white circular arrow indicates the direction of sound-energy flow. (c) Scheme of the superlattice composed of SC-C and SC-D with interfaces T-I and T-II. Red dotted rectangular box depicts a magnified view of interfaces T-I and T-II. (d) Projected band structure of the supercell (c) around the double-degenerate point. Black dots represent bulk bands. (e) Scheme of the superlattice composed of SC-C and SC-D with interfaces T-III and T-IV. Red dotted rectangular box depicts a magnified view of interfaces T-III and T-IV. (f) Band structure of the supercell (e) around the double-degenerate point.

APPENDIX E: EIGENMODE SYMMETRY AND TRANSMISSION CHARACTERISTICS

1. Eigenmodes and acoustic transport along interface I

There are three frequency bands, ES-I-1, ES-I-2, and ES-I-3, composed of topological states on interface I, and the eigenmodes of the edge states above them have obvious symmetry. For the convenience of expression, we define the sound-pressure mode as “1” for the symmetry of the coordinate axis and “0” for the antisymmetry of the coordinate axis. Therefore, the symmetry of the sound-pressure mode for the third and fourth edge-state bands at higher frequency is the same, and it is marked as “11.” The first and second numbers indicate symmetry about the x axis and y axis, respectively. The symmetry of the sound-pressure mode in the first and second edge-state bands includes “00” and “01.” Different symmetries mean that there are also differences in the transport characteristics of the edge states. We consider three plane waves with different frequencies incident in three directions into the acoustic field domain containing interface I (indicated by the green dotted line); as shown in Fig. 11, the incident frequencies of the first, second, and third rows are 2978.3, 3535.7, and 4031.4 Hz, respectively. The frequencies in the first and second lines are the frequencies of A_2 ($A_2{}'$) and B_2 ($B_2{}'$) when $k = 0.5$ (1.5) in band ES-I-1 (ES-I-2), and the third line is the frequency of E when $k = 0.1$ in band ES-I-3. Each column in the figure represents incident waves in the same direction. In the first column, the wave direction is [1, 0, 0], which shows that the transmission of a wave with the frequency of two edge states (with sound-pressure-mode symmetry of 00 or 01) is suppressed, while the higher frequency (acoustic-pressure-mode symmetry of the edge states is 11) can achieve acoustic transmission. For the case where the sound-pressure symmetry is 00 or 01, the direction of the sound-pressure modes is perpendicular to the incident direction, so it cannot be excited by this plane wave. Therefore, relative to the incident direction [1, 0, 0], the frequency band formed by the edge states with lower frequency cannot be excited. However, for the edge state with higher frequency, due to the symmetry about the x axis, this means that its eigenmode has a similar symmetry to be excited by the plane wave incident along the x-axis direction. From the second and third columns, when the wave-vector direction is along the y axis, including wave directions [0, 1, 0] and [0, −1, 0], and incident waves of different frequencies can propagate along the interface. This is because the acoustic pressure modes of the lower-frequency edge states are antisymmetric about the x axis, that is, the normal direction of the isophase plane is parallel to the y axis, so the plane waves propagating along the y axis can excite these modes, thereby realizing the

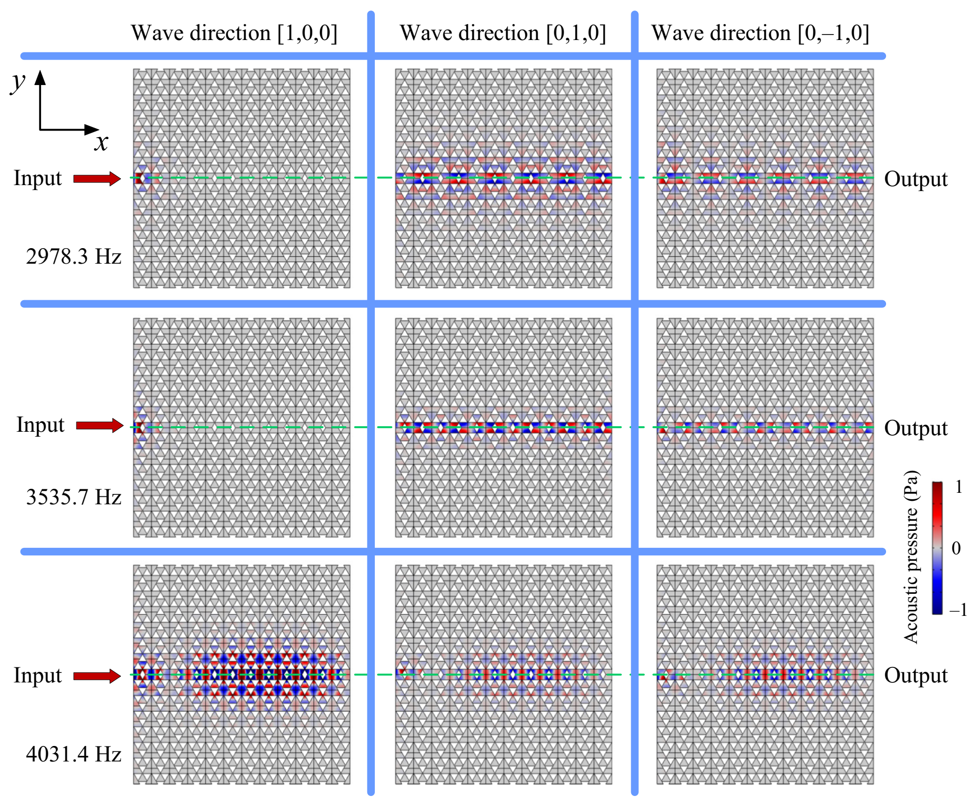

FIG. 11. Transmission of incident waves with different wave-vector directions incident on the sound-field domain containing interface I at frequencies of edge states A_2 ($A_2{}'$), B_2 ($B_2{}'$), and E.

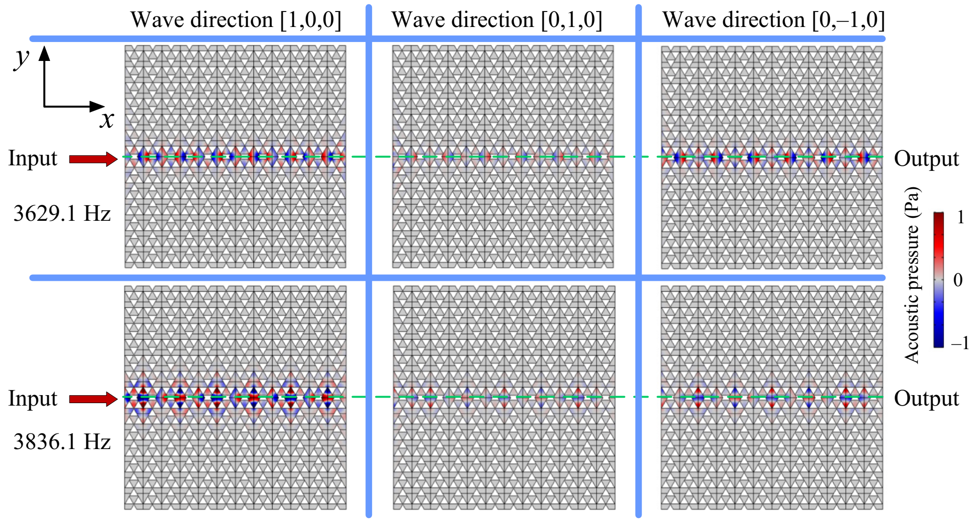

FIG. 12. Sound transmission along interface III with impinging waves coming from different directions with frequencies corresponding to edge states A_1 ($A_1{}'$) and B_1 ($B_1{}'$).

propagation of sound waves. It is worth noting that, for a plane wave with a frequency of 4031.4 Hz, the wave vector can propagate in the sound field no matter whether it is along the y axis or along the x axis, but the propagation loss is different.

2. Eigenstates on interface III and acoustic wave transmission

The edge states on interface III have the same symmetry, denoted by 11 (symmetric with respect to both X-Z and Y-Z planes). Sound propagation with wave vectors incident along three different directions is shown in Fig. 12, where the green dotted line indicates interface III. The frequencies correspond to edge states with $k = 0.5$ (1.5), corresponding to modes A_1 ($A_1{}'$) and B_1 ($B_1{}'$). It is observed that waves are transmitted along interface III, but their transmission loss is different for the different impinging directions. This result can be understood by looking at the pressure patterns of the edge modes shown in Fig. 5, where the sound-pressure modes on interface III are represented. It can be shown that the 0-Pa sound-pressure contour line on the interface is not parallel to the coordinate axis, so the normal line of the sound-pressure isophase plane has components along both the x axis and y axis, and the two quantities are different.

3. Edge states localized at interface II (IV) and acoustic wave transmission

For the case of edge states associated with interfaces II and IV, they do not exhibit any defined symmetry about the X-Z or Y-Z planes and, therefore, the propagation of impinging waves along different directions cannot be predicted by analyzing the symmetry of the eigenmodes. Figure 13 shows the transmission of incident plane waves with frequencies of 2985.9 and 3866.7 Hz. The incident directions from the first row to the third row are [−1, 0, 0], [1, 0, 0], and [0, 1, 0], respectively. The first two columns represent the propagation of sound waves along interface II, while the last two columns represent the propagation of sound waves across interface IV. In an acoustic field containing different interfaces, when the frequency of the incident wave is higher, the transmission of the acoustic wave on the interface is hardly affected by the direction of the incident wave. However, for the frequencies of lower-edge states, the acoustic wave transmission exhibits a correlation with the incident-wave direction. For example, for an incident wave with a frequency of 2985.9 Hz, when it propagates in the acoustic field domain including interface II, the transmission of wave direction [1, 0, 0] is suppressed. In the acoustic field domain containing interface IV, the transmission of wave direction [−1, 0, 0] is suppressed. This phenomenon can be used to design directional topological acoustic emission.

4. Deaf bands and transmission

From the pressure-field patterns of edge modes in Fig. 5, we observe that each mode exhibits different symmetry. Particularly, the modes in bands ES-I-1 and ES-I-2 have the planes of equal phase along the perpendicular y direction. Therefore, these modes cannot be excited by impinging waves traveling along the [1, 0, 0] direction, as shown in Fig. 11. Therefore, the modes in bands ES-I-1 and ES-I-2 can be considered as deaf acoustic modes [59] for waves propagating along the [1, 0, 0] direction.

It should be noted that, when the incident wave is not symmetric concerning the interface, the incident wave can generate additional non-negligible components in the transverse direction to the interface, allowing the

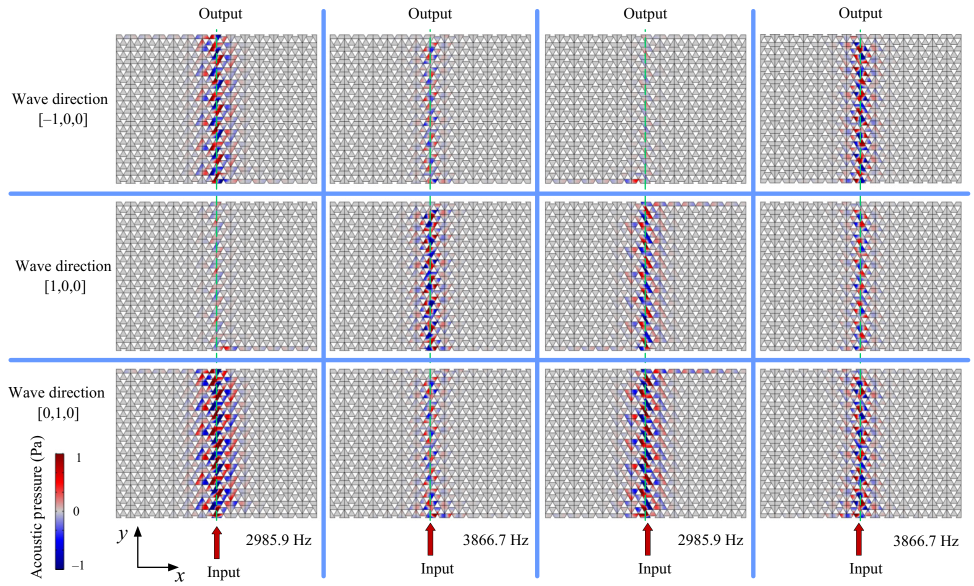

FIG. 13. Snapshots of the sound transmission along interface II (IV) produced by plane waves with different incident directions. Frequencies correspond to edge states A_3 (A_4) and B_3 (B_4).

excitation of deaf edge modes. This effect is shown in Fig. 14, where the excitation of an edge state with an impinging wave along the [1, 0, 0] direction is observed. Figure 14(a) shows the configuration when the excitation source is symmetric concerning the interface. With this configuration, Fig. 14(b) shows that the edge mode with a frequency of 3600 Hz cannot be excited, since its symmetry is orthogonal with respect to the symmetry of the impinging beam. However, when the exciting beam is shifted up, when entering the acoustic field, an effective component perpendicular to the initial incident-wave vector is generated, so that the incident wave in the deaf band in the x-axis direction can move along interface I, as shown in Fig. 14(d). When the incident plane wave (the line source is used in the simulation; the domain source here is a schematic diagram) is symmetrical about the interface. In other words, when the interface passes through the center of the incident-line source, the incident field does not generate the effective component perpendicular to the vector of the initial incident wave, before propagating along the interface. So, the incident wave is localized at the entrance. When the interface deviates from the center of the line source, an effective component perpendicular to the interface is generated in the incident acoustic field, so the intrinsic acoustic pressure mode on interface I is excited, and the topologically protected transmission of the edge state is realized. Therefore, the transmission through edge states belonging to deaf bands can be realized by changing the position of the incident sound field, thus turning the deaf modes into transmitted modes.

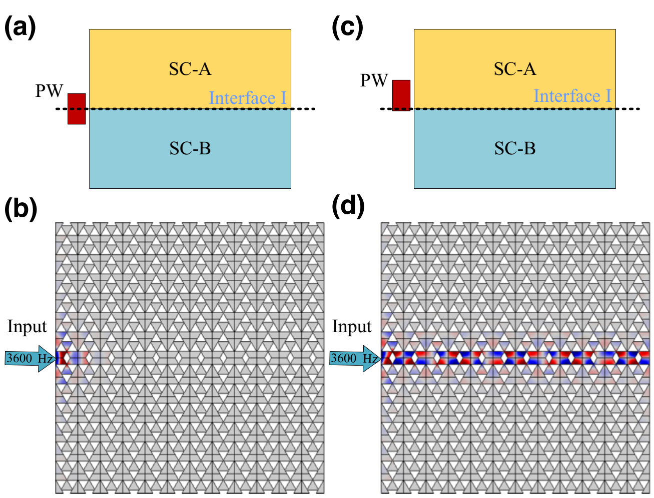

FIG. 14. (a) Scheme of the structure defining interface I, where the exciting beam (PW) is symmetric with respect to the interface. (b) Snapshot of the total-pressure pattern obtained with the previous configuration when the incident beam has a frequency of 3600 Hz. (c) Scheme of the structure defining interface I, where the exciting beam (PW) is nonsymmetric with respect to the interface. (d) Snapshot of the total pressure obtained with the previous configuration at a frequency of 3600 Hz. Now the deaf edge mode has been excited due to the asymmetry of the impinging beam.

APPENDIX F: TRANSPORT ALONG INTERFACES CONTAINING TOPOLOGICAL EDGE STATES

The paramount property of nontrivial topological systems is the exhibition of unidirectional and robust propagation with edge states existing at the interfaces between distinct topological phase zones. As described in Appendix E, the symmetry of the pressure patterns of the edge states enriches the transmission features through topological edge modes. On the other hand, some asymmetric scattering, producing an effective component perpendicular to the incident-wave vector, can easily modify the incident exciting plane wave. Therefore, when 2D plane waves impinge on the structure through the four different interfaces, a variety of behaviors in transmission appear, depending on the incident directions.

The chart shown in Fig. 15 reports the transmission properties of plane waves impinging on different ports, where letters Y and N indicate that the transmission is allowed and not, respectively. The number 0 indicates that no edge state with such a frequency exists at the corresponding interface. Therefore, the chart presents a comprehensive study of the transmission properties along the interfaces.

Physically, if the frequencies of the edge states are the same and the equal-phase planes of eigenmodes are not perpendicular to the direction of the incident wave, the edge states on both interfaces can be excited [59], realizing the phenomenon of topological state transport along different interfaces. Based on this, we investigate the case of sound-wave propagation along different interfaces. The bands of edge states localized on interface II (IV) and the bands of the edge states localized on interface I or interface III overlap, as shown in Fig. 16(a). Thus, we take port II (corresponding to interface II) as the incident end of the plane wave and study the transmission of port I (corresponding to interface I), port III (corresponding to interface III), and port IV (corresponding to interface IV), as shown in Fig. 16(b). When the frequency range of the incident wave is from 2930 to 4080 Hz, the transmission spectra at the three ports are shown in Fig. 16(c), in which the green line, blue line, and orange line represent the transmission spectra of port I, port III, and port IV, respectively. There are two frequency intervals of the edge states localized on interface II, as represented by blue shading and gray shading, respectively. In the blue-shaded area, there is acoustic transmission at both port I and port IV, and the transmission loss at port II is smaller than that at port IV, due to the wave in interface II first activating the edge states on interface I at the interface junction, and then the sound wave can propagate to interface IV. The black circle in the figure acts as a defect, which can increase additional scattering without affecting the transport of the topological state. In the gray-shaded area, there is acoustic wave transmission at both port III and port IV, and the transmission of both is similar in the overlapping-frequency band of the edge states, and the transmission loss is large, which is due to the small group velocity of the bands of the edge states.

APPENDIX G: FREQUENCY SHIFT OF EDGE STATES DUE TO ROD SIZE

The sample fabricated by a 3D printer shrinks to a certain extent after cooling, so the actual size of the rods was slightly smaller than that resulting from the design process ($R = 0.54a$), which led to small differences

	EG-A			EG-C			EG-E			EG-F		
Port I = Input	Port II	Port III	Port IV	Port II	Port III	Port IV	Port II	Port III	Port IV	Port II	Port III	Port IV
[1, 0,0]	*N*	*N*	*N*	*N*	*N*	*N*	0	0	0	0	0	0
[0, 1,0]	*Y*	*N*	*Y*	*N*	*Y*	*N*	0	0	0	0	0	0
[0, –1,0]	*Y*	*N*	*Y*	*N*	*Y*	*N*	0	0	0	0	0	0
	EG-A			EG-C			EG-E			EG-F		
Port II = Input	Port I	Port III	Port IV	Port I	Port III	Port IV	Port I	Port III	Port IV	Port I	Port III	Port IV
[0, 1,0]	*Y*	*N*	*Y*	0	0	0	*N*	*Y*	*Y*	*N*	*N*	*Y*
[1, 0,0]	*Y*	*N*	*Y*	0	0	0	*N*	*Y*	*Y*	*N*	*N*	*Y*
[–1, 0,0]	*Y*	*N*	*Y*	0	0	0	*N*	*Y*	*Y*	*N*	*N*	*Y*
	EG-A			EG-C			EG-E			EG-F		
Port III = Input	Port I	Port II	Port IV	Port I	Port II	Port IV	Port I	Port II	Port IV	Port I	Port II	Port IV
[–1, 0,0]	0	0	0	*Y*	*N*	*N*	*N*	*Y*	*Y*	0	0	0
[0, 1,0]	0	0	0	*Y*	*N*	*N*	*N*	*Y*	*Y*	0	0	0
[0, –1,0]	0	0	0	*Y*	*N*	*N*	*N*	*Y*	*Y*	0	0	0

FIG. 15. Chart of the transmission properties, where letters “Y” and “N” indicate if the transmission is allowed or not, respectively. Value “0” means no propagation.

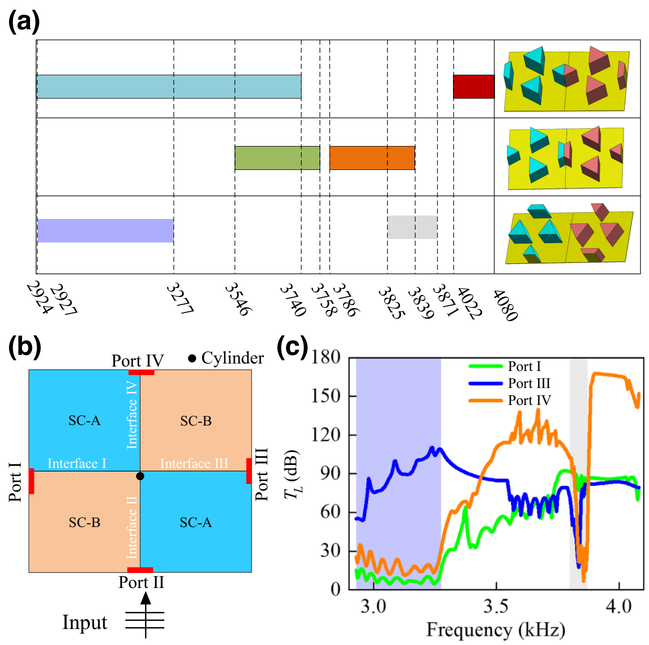

FIG. 16. (a) Frequency spectra of the topologically protected edge states. (b) Scheme of a SC structure made of SC-A and SC-B containing four interfaces. (c) Transmission loss (T_L) for waves transmitted along a path composed of different interfaces. Green line, blue line, and orange line represent the transmission spectra of port I, port III, and port IV, respectively. Blue- (gray-) shaded stripe represents the frequency interval of the edge states on interface II (IV).

between the numerical simulations and the experimental results. For example, $R = 0.51a$ is considered here in Fig. 17(a), and the dispersion relation of the supercell containing interface II is shown in Fig. 17(b), where the blue and orange lines define the frequency bands containing topological states. These two bands have bandwidths like those obtained experimentally, as indicated by the shaded areas in Fig. 17(c). Therefore, we concluded that the frequency blueshift observed experimentally in Fig. 9(b) was attributed to the rod dimension, which was slightly smaller than that obtained in the design process.

APPENDIX H: EXPERIMENTAL SETUP

The rods of the sample are fabricated using ABS via 3D printing. The sample in Fig. 6(a) [Fig. 6(d)], which consisted of 108 (72) triangular rods, was embedded in a 2D planar waveguide formed by two Plexiglas plates. The height of the rods is 30 mm. In this case, the 2D approximation is applicable, due to the waveguide supporting the propagating mode uniformly along the rod axis for the wavelengths under consideration. Experiments were conducted with a linear array of 16 speakers, to create an incident beam with a Gaussian profile. The microphone is fixed to the coordinate position system and scans an area of 40×24 cm^2 at the output of the sample. Both the card (NI PXle-6259) for data acquisition from Mic-1 and the sound card (NI PXI-6723) to regulate the emission waves are integrated into the personal computer (computer). The scanning-frequency interval is 10 Hz.

APPENDIX I: DIRECTIONAL PROPAGATION AND FOCUSING

According to the simulations and experiments, the waves exiting the structure show obvious directionality. The underlying physics explaining such directional behavior comes from the eigenmodes defining the topological states on the interface. When the incident plane wave excites the eigenmodes at the interface, the pressure field

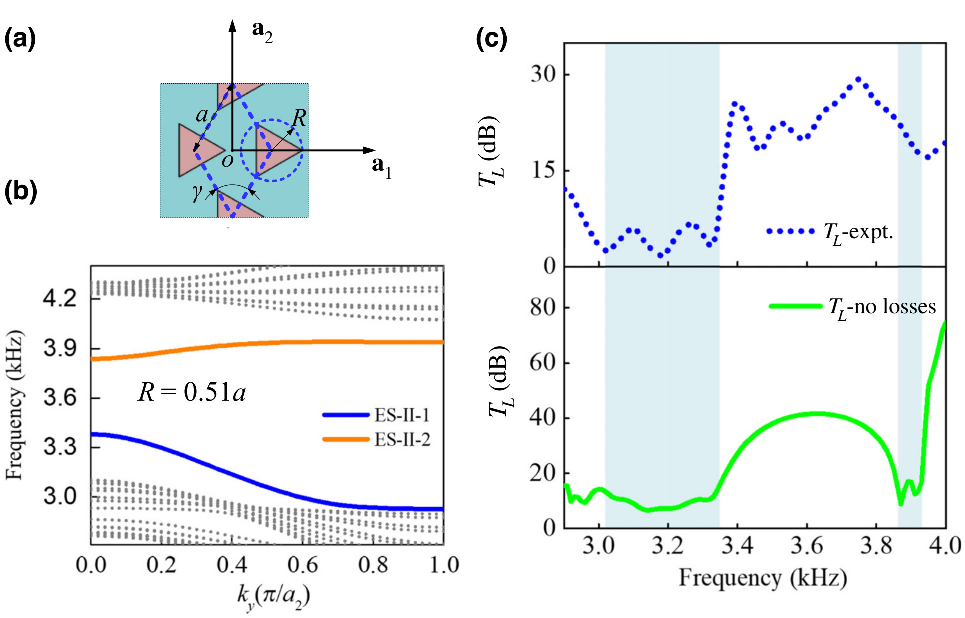

FIG. 17. (a) Scheme of the unit cell. Distance between rods is a, and the radius of the outer circle of the triangular rods is R. (b) Dispersion relation of the supercell containing interface II with $R = 0.51a$. Gray dots represent bulk modes. Blue and orange lines represent bands ES-II-1 and ES-II-2 composed of topological states, respectively. (c) Transmission loss (TL) obtained from experiments (upper panel) and numerical calculations (bottom panel). Green line represents numerical simulations in the inviscid approximation. Shaded regions define the bandwidths of bands ES-II-1 and ES-II-2.

is modulated by the eigenmodes, thus forming directional sound propagation.

Figure 18(a) schematically shows the directional property of the edge states at interface IV; when waves with a specific range of frequencies propagate along interface IV to the outer field, the sound waves exhibit a principal propagation direction at a certain angle, δ. For example, for a frequency of 3060 Hz, Fig. 18 shows the experimental 2D map of the absolute pressure measured in the scanned area behind the sample. This measurement confirms the theoretical prediction and simulations. Figure 18(c) depicts the absolute value of pressure along different angles δ. The different lines are extracted from the experimental 2D map shown in Fig. 18(b). It is observed that the radiated wave has a principal beam along 30°. Small side lobes appear at 60° and 90°. There are also components along $\delta = 150°$ and 120°, but they can be neglected in comparison with the case at an angle of 30°.

The frequencies of edge states at interfaces IV and II are the same, but the orientation of the triangular scatterers is interchanged along the interface. These features can be exploited to design an acoustic focusing device, as schematically outlined in Fig. 18(d). It is observed how the proposed sandwiched structure is composed of SC-A and SC-B and contains interfaces IV and II. Thus, it is expected that the waves radiating from the interfaces will interfere, producing a focal point (red dot) in the radiation field. The simulation results of a 4×4 sandwich structure for the absolute pressure of a wave with a frequency of 3050 Hz are shown in Fig. 18(e), where a focal area is clearly shown in the radiation field. In addition, Fig. 18(f) shows a comparison between the profiles of the radiation field

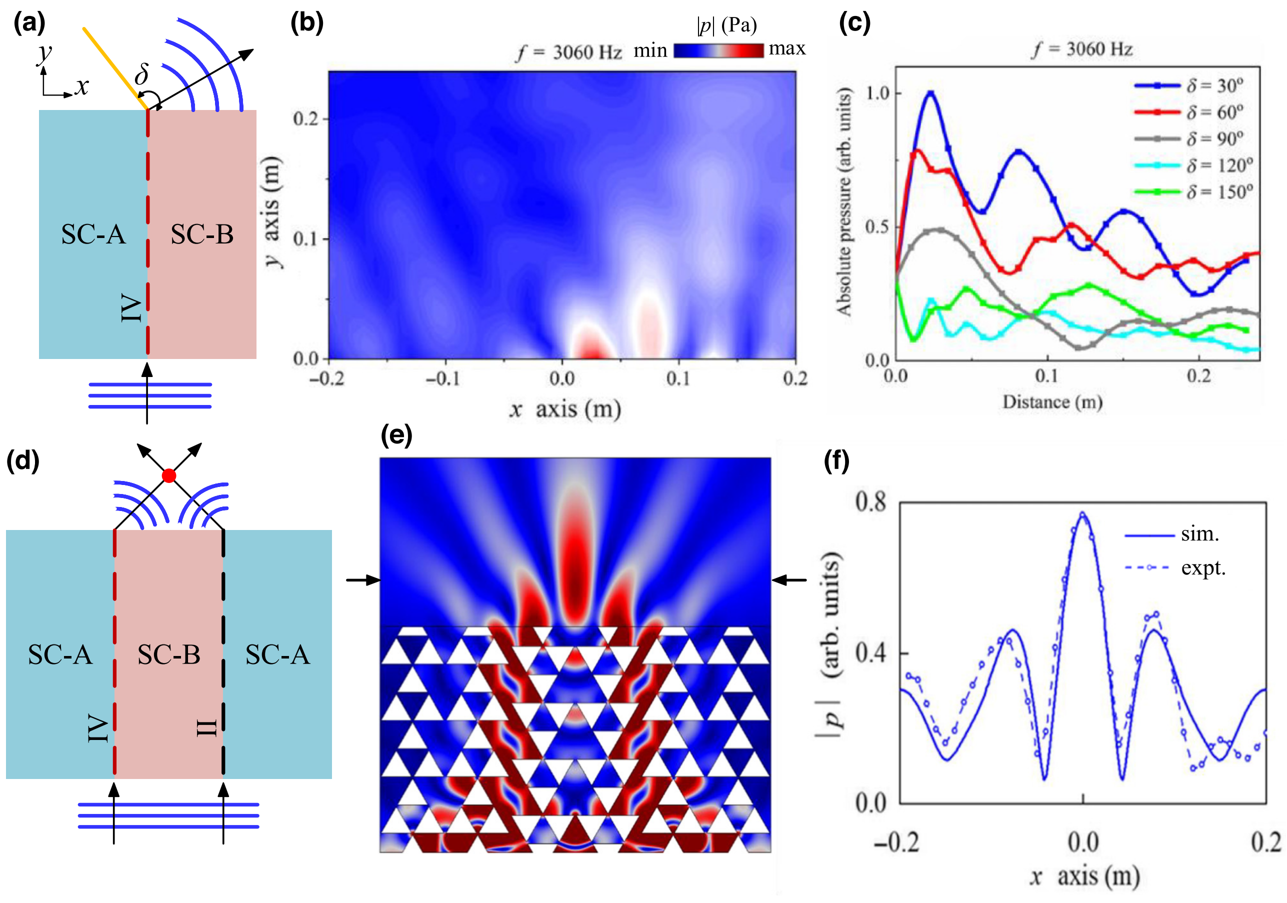

FIG. 18. (a) Schematic diagram representing the propagation of a planar wave front impinging on a structure containing interface IV. Horizontal blue lines represent the impinging wave front; red dotted line represents the excited edge state, while the arrow, which forms an angle of δ with the x axis, represents the main propagation direction. (b) Snapshot of the absolute-pressure map measured in the scanned area using waves with a frequency of 3060 Hz. (c) Absolute pressure measured along different output directions δ obtained from the map in (b). (d) Schematic diagram of the acoustic focusing device containing interfaces II and IV. (e) Numerical simulations showing the focusing produced by an incident plane wave at 3050 Hz propagating through the sandwiched structure in (d). Color scale represents the absolute pressure. (f) Profile of the absolute pressure along the line defined by the arrows in (e). Dashed line with symbols and the continuous line represent the experimental and simulated profiles, respectively. For a better comparison, experimental data are normalized to the peak value found in the simulations.

along the line passing through the focal point. The black arrows in Fig. 18(e) define such a line. Note that there is good agreement between the experimental (blue symbols) and simulated (blue continuous line) profiles, supporting the possibility of obtaining focusing devices from topologically protected edge states. In addition to phononic crystals with an external lenticular shape [11], gradual material dispersion with gradual geometrically curved surfaces [61–64], and gradient refractive indices in artificial focusing devices [65,66], using the directivity of edge states can also be an effective way to achieve focusing.

[1] D. J. Thouless, M. Kohmoto, M. P. Nightingale, and M. Den Nijs, Quantized Hall conductance in a two-dimensional periodic potential, Phys. Rev. Lett. **49**, 405 (1982).
[2] K. V. Klitzing, G. Dorda, and M. Pepper, New method for high-accuracy determination of the fine-structure constant based on quantized Hall resistance, Phys. Rev. Lett. **45**, 494 (1980).
[3] C. L. Kane and E. J. Mele, Quantum spin Hall effect in graphene, Phys. Rev. Lett. **95**, 226801 (2005).
[4] J. E. Moore, The birth of topological insulators, Nature **464**, 194 (2010).
[5] Y. L. Chen, J. G. Analytis, J.-H. Chu, Z. K. Liu, S.-K. Mo, X. L. Qi, H. J. Zhang, D. H. Lu, X. Dai, Z. Fang, *et al.*, Experimental realization of a three-dimensional topological insulator, Bi_2Te_3, Science **325**, 178 (2009).
[6] W. Yao, D. Xiao, and Q. Niu, Valley-dependent optoelectronics from inversion symmetry breaking, Phys. Rev. B **77**, 235406 (2008).
[7] G. W. Semenoff, V. Semenoff, and F. Zhou, Domain walls in gapped graphene, Phys. Rev. Lett. **101**, 087204 (2008).
[8] Long Ju, Zhiwen Shi, Nityan Nair, Yinchuan Lv, Chenhao Jin, Jairo Velasco Jr, Claudia Ojeda-Aristizabal, Hans A. Bechtel, Michael C. Martin, Alex Zettl, James Analytis, and Feng Wang, Topological valley transport at bilayer graphene domain walls, Nature **520**, 650 (2015).
[9] L. Fu, Topological crystalline insulators, Phys. Rev. Lett. **106**, 106802 (2011).
[10] L. Fu, C. L. Kane, and E. J. Mele, Topological insulators in three dimensions, Phys. Rev. Lett. **98**, 106803 (2007).
[11] A. A. Burkov, Topological semimetals, Nat. Mater. **15**, 1145 (2016).
[12] S. Murakami, M. Hirayama, R. Okugawa, and T. Miyake, Emergence of topological semimetals in gap closing in semiconductors without inversion symmetry, Sci. Adv. **3**, 1602680 (2017).
[13] Y. Wang, H.-X. Wang, L. Liang, W. Zu, L. Fan, Z.-K. Lin, F. Li, X. Zhang, P.-G. Luang, Y. Poo, *et al.*, Hybrid topological photonic crystals, Nat. Commun. **14**, 4457 (2023).
[14] L. H. Wu and X. Hu, Scheme for achieving a topological photonic crystal by using dielectric material, Phys. Rev. Lett. **114**, 223901 (2015).
[15] Ziteng Wang, Xiangdong Wang, Zhichan Hu, Domenico Bongiovanni, Dario Jukić, Liqin Tang, Daohong Song, Roberto Morandotti, Zhigang Chen, and Hrvoje Buljan, Sub-symmetry-protected topological states, Nat. Phys. **19**, 992 (2023).
[16] L. Lu, C. Fang, L. Fu, S. G. Johnson, J. D. Joannopoulos, and M. Soljačić, Symmetry-protected topological photonic crystal in three dimensions, Nat. Phys. **12**, 337 (2016).
[17] X. C. Sun, H. Chen, H. S. Lai, C. H. Xia, C. He, and Y. F. Chen, Ideal acoustic quantum spin Hall phase in a multi-topology platform, Nat. Commun. **14**, 952 (2023).
[18] Z. Yang, F. Gao, X. Shi, X. Lin, Z. Gao, Y. Chong, and B. Zhang, Topological acoustics, Phys. Rev. Lett. **114**, 114301 (2015).
[19] R. Fleury, D. L. Sounas, C. F. Sieck, M. R. Haberman, and A. Alù, Sound isolation and giant linear nonreciprocity in a compact acoustic circulator, Science **343**, 516 (2014).
[20] S. Yves, X. Ni, and A. Alu, Topological sound in two dimensions, Ann. N. Y. Acad. Sci. **1517**, 63 (2022).
[21] Z. Huang, J. Wu, C. Wang, S. Yang, and F. Ma, Resonant-scattering hybrid device for multiband acoustic topology valley transmission, Phys. Rev. B **104**, 094110 (2021).
[22] J. Lu, C. Qiu, W. Deng, X. Huang, F. Li, F. Zhang, S. Chen, and Z. Liu, Valley topological phases in bilayer sonic crystals, Phys. Rev. Lett. **120**, 116802 (2018).
[23] C. Xu, Z. G. Chen, G. Zhang, G. Ma, and Y. Wu, Multi-dimensional wave steering with higher-order topological phononic crystal, Sci. Bull. **66**, 1740 (2021).
[24] R. Süsstrunk and S. D. Huber, Observation of phononic helical edge states in a mechanical topological insulator, Science **349**, 47 (2015).
[25] X. Ni, S. Yves, A. Krasnok, and A. Alu, Topological metamaterials, Chem. Rev. **123**, 7585 (2023).
[26] S. D. Huber, Topological mechanics, Nat. Phys. **12**, 621 (2016).
[27] L. Xin, Y. Siyuan, L. Harry, L. Minghui, and C. Yanfeng, Topological mechanical metamaterials: A brief review, Curr. Opin. Solid State Mater. Sci. **24**, 100853 (2020).
[28] Xiaoxiao Wu, Xin Li, Ruo-Yang Zhang, Xiao Xiang, Jingxuan Tian, Yingzhou Huang, Shuxia Wang, Bo Hou, C. T. Chan, and Weijia Wen, Deterministic scheme for two-dimensional type-II Dirac points and experimental realization in acoustics, Phys. Rev. Lett. **124**, 075501 (2020).
[29] Z. W. Zhang, Y. Tian, Y. Cheng, Q. Wei, X. J. Liu, and J. Christensen, Topological acoustic delay line, Phys. Rev. Appl. **9**, 034032 (2018).
[30] J. Y. Lu, C. Y. Qiu, S. J. Xu, Y. T. Ye, M. Z. Ke, and Z. Y. Liu, Dirac cones in two-dimensional artificial crystals for classical waves, Phys. Rev. B **89**, 134302 (2014).
[31] Tomoki Ozawa, Hannah M. Price, Alberto Amo, Nathan Goldman, Mohammad Hafezi, Ling Lu, Mikael Rechtsman, David Schuster, Jonathan Simon, Oded Zilberberg, and Iacopo Carusotto, Topological photonics, Rev. Mod. Phys. **91**, 015006 (2019).
[32] Y. F. Chen, Z. G. Chen, H. Ge, C. He, X. Li, M. H. Lu, X. C. Sun, S. Y. Yu, and X. Zhang, Various topological phases and their abnormal effects of topological acoustic metamaterials, Interdiscip. Mater. **2**, 179 (2023).
[33] K. Sakoda, Proof of the universality of mode symmetries in creating photonic Dirac cones, Opt. Express **20**, 25181 (2012).
[34] A. B. Khanikaev, R. Fleury, S. H. Mousavi, and A. Alu, Topologically robust sound propagation in an

angular-momentum-biased graphene-like resonator lattice, Nat. Commun. **6**, 8260 (2015).
[35] J. Y. Lu, C. Y. Qiu, L. P. Ye, X. Y. Fan, M. Z. Ke, F. Zhang, and Z. Y. Liu, Observation of topological valley transport of sound in sonic crystals, Nat. Phys. **13**, 369 (2016).
[36] J. Lu, C. Qiu, M. Ke, and Z. Liu, Valley vortex states in sonic crystals, Phys. Rev. Lett. **116**, 093901 (2016).
[37] Z. Zhang, Q. Wei, Y. Cheng, T. Zhang, D. Wu, and X. Liu, Topological creation of acoustic pseudospin multipoles in a flow-free symmetry-broken metamaterial lattice, Phys. Rev. Lett. **118**, 084303 (2017).
[38] C. He, X. Ni, H. Ge, X. C. Sun, Y.-B. Chen, M.-H. Lu, X.-P. Liu, and Y.-F. Chen, Acoustic topological insulator and robust one-way sound transport, Nat. Phys. **12**, 1124 (2016).
[39] H. Xue, Y. Yang, and B. Zhang, Topological acoustics, Nat. Rev. Mater. **7**, 974 (2022).
[40] K. Suzuki, X-ray studies on precipitation of metastable centers in mixed crystals NaCl-CdCl, J. Phys. Soc. Jpn. **16**, 67 (1961).
[41] D. Caballero, J. Sánchez-Dehesa, R. Martínez-Sala, C. Rubio, J. V. Sánchez-Pérez, L. Sanchis, and F. Meseguer, Suzuki phase in two-dimensional sonic crystals, Phys. Rev. B **64**, 064303 (2001).
[42] K. Sakoda, Double Dirac cones in triangular-lattice metamaterials, Opt. Express **20**, 9925 (2012).
[43] G. G. Pyrialakos, N. Schmitt, N. S. Nye, M. Heinrich, N. V. Kantartzis, A. Szameit, and D. N. Christodoulides, Symmetry-controlled edge states in the type-II phase of Dirac photonic lattices, Nat. Commun. **11**, 2074 (2020).
[44] C. K. Chiu, Y. H. Chan, X. Li, Y. Nohara, and A. P. Schnyder, Type-II Dirac surface states in topological crystalline insulators, Phys. Rev. B **95**, 035151 (2017).
[45] D. Jia, H. X. Sun, J. P. Xia, S.-q. Yuan, X.-j. Liu, and C. Zhang, Acoustic topological insulator by honeycomb sonic crystals with direct and indirect band gaps, New J. Phys. **20**, 093027 (2018).
[46] Z. Huang, J. H. Wu, Y. Huang, C. Liu, C. Chen, and F. Ma, Multi-band selective acoustic valley transport through band separation of topological interface states, J. Phys. D: Appl. Phys. **55**, 045301 (2021).
[47] B. Z. Xia, T. T. Liu, G. L. Huang, H. Q. Dai, J. R. Jiao, X. G. Zang, D.-J. Yu, S.-J. Zheng, and J. Liu, Topological phononic insulator with robust pseudospin-dependent transport, Phys. Rev. B **96**, 094106 (2017).
[48] M. Xiao, G. C. Ma, Z. Y. Yang, P. Sheng, Z. Q. Zhang, and C. T. Chan, Geometric phase and band inversion in periodic acoustic systems, Nat. Phys. **11**, 240 (2015).
[49] H. X. Wang, G. Y. Guo, and J. H. Jiang, Band topology in classical waves: Wilson-loop approach to topological numbers and fragile topology, New J. Phys. **21**, 093029 (2019).
[50] T. Fukui, Y. Hatsugai, and H. Suzuki, Chern numbers in discretized Brillouin zone: Efficient method of computing (spin) Hall conductances, J. Phys. Soc. Jpn. **74**, 1674 (2005).
[51] R. Zhao, G. D. Xie, M. L. N. Chen, Z. Lan, Z. Huang, and W. E. I. Sha, First-principle calculation of Chern number in gyrotropic photonic crystals, Opt. Express **28**, 4638 (2020).
[52] A. Bouhon, A. M. Black-Schaffer, and R. J. Slager, Wilson loop approach to fragile topology of split elementary band representations and topological crystalline insulators with time-reversal symmetry, Phys. Rev. B **100**, 195135 (2019).
[53] Z. Huang, J. H. Wu, Y. Z. Lei, C. R. Liu, and F. Y. Ma, Multi-band acoustic topological insulator, Mater. Today Phys. **27**, 100793 (2022).
[54] Z. Zhang, Y. Tian, Y. Wang, S. Gao, Y. Cheng, X. Liu, and J. Christensen, Directional acoustic antennas based on valley-Hall topological insulators, Adv. Mater. **30**, 1803229 (2018).
[55] Z. Zhang, Y. Cheng, and X. Liu, Achieving acoustic topological valley-Hall states by modulating the subwavelength honeycomb lattice, Sci. Rep. **8**, 16784 (2018).
[56] F. Zhang, J. Jung, G. A. Fiete, Q. Niu, and A. H. MacDonald, Spontaneous quantum Hall states in chirally stacked few-layer graphene systems, Phys. Rev. Lett. **106**, 156801 (2011).
[57] K. F. Mak, K. L. McGill, J. Park, and P. L. McEuen, The valley Hall effect in MoS2 transistors, Science **344**, 1489 (2014).
[58] X. J. Zhang, M. Xiao, Y. Cheng, M.-H. Lu, and J. Christensen, Topological sound, Commun. Phys. **1**, 97 (2018).
[59] J. V. Sánchez-Pérez, D. Caballero, R. Mártinez-Sala, C. Rubio, J. Sánchez-Dehesa, F. Meseguer, J. Llinares, and F. Gálvez, Sound attenuation by a two-dimensional array of rigid cylinders, Phys. Rev. Lett. **80**, 5325 (1998).
[60] J. Sánchez-Dehesa and J. R. Arias-Gonzalez, Characterization of avoided crossings in acoustic superlattices: The Shannon entropy in acoustics, Front. Phys. **10**, 971171 (2022).
[61] F. Y. Ma, Z. Huang, C. R. Liu, and J. H. Wu, Acoustic focusing and imaging via phononic crystal and acoustic metamaterials, J. Appl. Phys. **131**, 011103 (2022).
[62] W. J. Toulis, Acoustic focusing with spherical structures, J. Acoust. Soc. Am. **35**, 286 (1963).
[63] C. A. Boyles, Radiation characteristics of spherically symmetric, perfect focusing acoustic lenses, J. Acoust. Soc. Am. **45**, 351 (1969).
[64] J. M. Heritier, J. E. Fouquet, and A. E. Siegman, Photoacoustic cell using elliptical acoustic focusing, Appl. Opt. **21**, 90 (1982).
[65] S. A. Cummer, J. Christensen, and A. Alù, Controlling sound with acoustic metamaterials, Nat. Rev. Mater. **1**, 1 (2016).
[66] G. C. Ma and P. Sheng, Acoustic metamaterials: From local resonances to broad horizons, Sci. Adv. **2**, 1501595 (2016).